Experimental and theoretical study of anomalous temperature dependence of phonons in $Y_2Ti_2O_7$ pyrochlore

P. K. Verma,[1,*] Surajit Saha,[2,†] D. V. S. Muthu,[3] Surjeet Singh,[4] R. Suryanarayanan,[5] A. Revcolevschi,[5] U. V. Waghmare,[6] A. K. Sood,[3] and H. R. Krishnamurthy[3]

[1]*Department of Chemistry, Indian Institute of Science Education and Research Bhopal, Bhopal 462066, India*
[2]*Department of Physics, Indian Institute of Science Education and Research Bhopal, Bhopal 462066, India*
[3]*Department of Physics, Indian Institute of Science Bangalore, Bangalore 560012, India*
[4]*Department of Physics, Indian Institute of Science Education and Research Pune, Pune 411008, India*
[5]*Université Paris-Sud, Laboratoire de Physico-Chimie de l'Etat Solide, ICMMO, UMR8182, CNRS, Bâtiment 414, Orsay, France*
[6]*Theoretical Sciences Unit, Jawaharlal Nehru Centre for Advanced Scientific Research Bangalore, Bangalore 560064, India*

(Received 22 March 2022; revised 26 July 2022; accepted 22 September 2022; published 7 October 2022)

We present Raman spectroscopic as well as first-principles theoretical studies of the temperature dependence of phonon spectra in the pyrochlore $Y_2Ti_2O_7$. Our experimental results show that the frequencies of several phonons display anomalous softening upon cooling. Our theoretical calculations of the temperature dependence, via phonon self-energy corrections arising from cubic anharmonic interactions, lead to such anomalies but only for a couple of high-frequency phonon modes. Our work strongly supports the suggestion that anharmonic phonon-phonon interactions are strong in the pyrochlore titanates and that they are responsible for the phonon anomalies observed. The strong anharmonic effects are likely due to the presence of the vacant Wyckoff sites and the shifts of the oxygen atoms from their actual positions in the pyrochlore lattice. However, the theoretical calculations fail to explain the anomalous behavior of low and intermediate frequency modes observed in our experiments. It seems likely that a much more sophisticated, perhaps nonperturbative, treatment of the anharmonic interactions will be required for a full explanation of the anomalies.

DOI: 10.1103/PhysRevB.106.144303

I. INTRODUCTION

Pyrochlores with the general formula $A_2B_2O_7$ accommodate a wide range of compositions due to their structural flexibility, leading to materials with a fascinating variety of properties [1–3]. For instance, their electronic transport can vary from highly insulating through semiconducting to metallic behavior depending on the chemical composition. Several rare-earth-based titanate pyrochlores display fascinating magnetic properties such as spin-liquid behavior in $Tb_2Ti_2O_7$ [4] and spin-ice behavior in $Dy_2Ti_2O_7$ [5] and $Ho_2Ti_2O_7$ [6] compounds. The properties of the magnetic pyrochlores, where Ru, Mn, or Mo is present at the *B* sites, and Gd, Er, Tb, Dy, or Sm is present at the *A* sites, vary from paramagnetic to ferromagnetic or antiferromagnetic behavior.

Recently, authors of extensive Raman and infrared (IR) spectroscopy studies of several pyrochlore compounds have unravelled various important properties involving structural changes as well as interactions between the lattice, crystalline electric field, and spin degrees of freedom [7–17]. For example, $Sm_2Ti_2O_7$, $Gd_2Ti_2O_7$, $Tb_2Ti_2O_7$, and $Yb_2Ti_2O_7$ undergo structural transitions under high pressure, as revealed by Raman and x-ray experiments [12–14,16]. The spin-ice compound $Dy_2Ti_2O_7$ shows a structural transition $<\sim$100 K [7] which may have an important role in its low-temperature magnetic phase. Furthermore, phonon spectra in several titanate pyrochlores ($A_2Ti_2O_7$, where A = Gd, Tb, Dy, Ho, Er, Yb, and Lu) show anomalies in their temperature dependence [7–11,16]. The anomalous temperature dependence of the properties of a few IR active phonons in $Dy_2Ti_2O_7$ was attributed to strong spin-phonon coupling by Bi *et al.* [11]. However, since the exchange interaction is rather weak for most pyrochlore titanates (ranging between $\sim$0.25 K in $Sm_2Ti_2O_7$ [15] to 19 K in $Tb_2Ti_2O_7$ [18,19]), and no long-range spin order has been seen in $Dy_2Ti_2O_7$, $Gd_2Ti_2O_7$, and $Er_2Ti_2O_7$ down to very low temperatures [20], this explanation has been questioned [9]. Furthermore, the phonon anomalies are unlikely to be due to the coupling between phonons and crystal-field excitations because $Gd_2Ti_2O_7$ exhibits comparable phonon anomalies [9] even though its crystal-field effects are rather weak, as the half-filled 4*f*-shells in its Gd^{3+} ions have spherical symmetry. We note that $Y_2Ti_2O_7$ (YTO) is a wide-bandgap semiconductor (with a bandgap of $\sim$3 eV). This rules out an electronic origin of anharmonicity and the phonon anomalies expected in metals [21].

In this paper, we present a temperature-dependent Raman spectroscopic study together with a first-principles density functional theory (DFT)-based study of the phonon spectra in the nonmagnetic titanate pyrochlore YTO. The experiments reveal an anomalous decrease or softening of the frequencies of several phonons upon cooling from room temperature down to 35 K. Our theoretical calculations of this temperature dependence, in terms of the phonon self-energy effects arising

*vpramod@iiserb.ac.in
†surajit@iiserb.ac.in

from the (DFT calculated) phonon-phonon interactions arising from cubic anharmonicity, lead to such anomalies, though only for a couple of high-frequency phonon modes. Our calculations include results for the Grüneisen parameters for several phonon modes, a detailed study of the phonon linewidths, and the contributions to the phonon frequency change due to quasiharmonic as well as cubic-anharmonic effects.

II. EXPERIMENTAL TECHNIQUES

Y_2O_3 (99.99%) and TiO_2 (99.99%) at the right stoichiometry were mixed thoroughly and heated at 1200 °C for ∼15 h. The resulting mixture was well ground and isostatically pressed into rods of ∼8 cm long and 5 mm diameter. These rods were sintered at 1400 °C in air for ∼72 h. This procedure was repeated until the compound YTO was formed, as revealed by powder x-ray diffraction analysis, with no traces of any secondary phase. These rods were then subjected to single-crystal growth by the floating-zone method in an IR image furnace under flowing oxygen. X-ray diffraction carried out on the powder obtained by crushing part of a single-crystalline sample and energy dispersive x-ray analysis on a scanning electron microscope indicated a pure pyrochlore YTO phase. The Läue back-reflection technique is used to orient the crystal along with the principal crystallographic directions.

Micro-Raman measurements on a (111)-oriented single crystal of YTO were performed using a continuous flow helium cryostat attached to a temperature controller (Oxford Instruments), using the 514.5 nm line of an Ar^+ ion laser (Coherent Innova 300) with ∼15 mW of power falling on the sample. The laser polarization was normal to the (111) crystallographic axis. The scattered light was collected and analyzed using a computer-controlled DILOR XY Raman spectrometer having three holographic gratings (1800 groves/mm) coupled to a liquid-nitrogen-cooled charged-coupled device CCD 3000 (Jobin Yvon-SPEX make) of pixel resolution 0.85 cm^{-1}. The instrument broadening is ∼5 cm^{-1}.

III. COMPUTATIONAL TECHNIQUES

Our DFT calculations [22,23] were carried out using the QUANTUM ESPRESSO code [24], with optimized norm-conserving Vanderbilt (ONCV) pseudopotentials [25,26]. The pseudopotentials were obtained from PSEUDODOJO. The local density approximation (LDA) [27] was used for the exchange-correlation energy functional. We used an energy cutoff of 80 Ry for the plane-wave basis sets. The **k**-points summation over the Brillouin zone (BZ) for the electronic energy calculations was implemented using the Monkhorst-Pack method with a $4 \times 4 \times 4$ special **k**-points mesh [28]. Density functional perturbation theory (DFPT) [29,30] calculations were carried out to obtain the phonon dispersions within the BZ. For this purpose, the dynamical matrices were evaluated for a grid of $2 \times 2 \times 2$ **q**-points. The Broyden-Fletcher-Goldfarb-Shanno minimization scheme [31] was employed to optimize the structure. The D3Q code [32] was used to calculate the cubic anharmonic interatomic force constants or, equivalently, the three-phonon coupling matrix elements [33–36].

IV. SYMMETRY CHARACTERISTICS OF PHONONS IN TITANATE PYROCHLORES

Pyrochlores belong to the face-centered cubic family (space group: $Fd\bar{3}m$) with 2 f.u. of ($A_2B_2O_7$) per primitive unit cell. A more precise specification of the formula unit is $A_2B_2O_6O'$, where the O corresponds to the oxygen atoms situated at the 48*f* Wyckoff sites, and O′ refers to the oxygen atoms situated at the 8*b* Wyckoff sites. There have been several theoretical and experimental studies of the vibrational modes in these systems [37–41]. The 66 phonon modes at the BZ center (Γ point) can be classified into 26 irreducible representations as follows:

$$F = A_{1g} + E_g + 2T_{1g} + 4T_{2g} + 3A_{2u} + 3E_u + 8T_{1u} + 4T_{2u}. \quad (1)$$

(Modes labeled A, E, and T are one-, two-, and threefold degenerate, respectively.) Out of these, only the A_{1g}, E_g, and $4T_{2g}$ modes are Raman active, while the T_{1u} modes are IR active. The remaining modes ($2T_{1g}$, $3A_{2u}$, $3E_u$, and $4T_{2u}$) are optically inactive. The above irreducible representations of the normal modes imply that the IR active modes involve the vibrations of all four nonequivalent sites (A, B, O, and O′) and are due to either bond stretching or angular bending. However, the Raman active modes involve the vibrations of the oxygen atoms only; the A and B atoms remain stationary because they occupy sites with inversion symmetry (site symmetry: D_{3d}). The Raman modes A_{1g}, E_g, and $3T_{2g}$ involve the vibrations of oxygen atoms located at 48*f* Wyckoff sites, whereas the fourth T_{2g} Raman mode arises from the vibrations of O′ atoms situated at the 8*b* sites.

In the pyrochlores, while the 8*b* sites are occupied by O′ atoms, the 8*a* sites are vacant. The A^{3+} ions form a tetrahedral network with an O′ atom at the center of each tetrahedron, while the B^{4+} ions form another tetrahedral network having the 8*a* vacant sites at the centers. Furthermore, in pyrochlores, the 48*f* site is occupied by O atoms whose position has an adjustable parameter x. The various ions in pyrochlores form a complex network of polyhedra whose shapes vary with the value of x, which ranges between 0.3125 ($\frac{5}{16}$) and 0.375 ($\frac{3}{8}$). When $x = 0.3125$, the B^{4+} ions form a perfect BO_6 octahedron, and the A^{3+} ions are coordinated by eight oxygen atoms ($6O + 2O'$). However, at the other extreme, for $x = 0.375$, the A^{3+} ions form a regular cube with eight oxygen atoms ($6O + 2O'$), while the BO_6 octahedron becomes distorted. Experimentally, the value of x is usually found to be within 0.320–0.345 and, therefore, the polyhedra formed by the A^{3+} and B^{4+} cations are distorted from the above ideal polyhedra. The value of x in the case of YTO is found to be 0.33. As discussed later, it seems likely that the presence of the empty 8*a* sites leads to relatively larger anharmonic interactions involving modes in which the ions at its neighboring sites, i.e., Ti^{4+} ions at the 16*c* site and O^{2-} ions at 48*f* site, vibrate.

V. PHONON SELF-ENERGY CALCULATIONS

Using standard quantum many-body perturbation theory techniques and to the second order in the three-phonon interactions arising from cubic anharmonicity, the imaginary part

of the phonon self-energy is given by [42–44]

$$\Gamma_j^{(3)}(\omega,T)=\frac{18\pi}{\hbar^2}\sum_{\mathbf{q},j_1,i_2}|V^{(3)}(\mathbf{0},j;\mathbf{q},j_1;-\mathbf{q},j_2)|^2(\{n[\omega_{j_1}(\mathbf{q})]+n[\omega_{j_2}(-\mathbf{q})]+1\}\{\delta[\omega-\omega_{j_1}(\mathbf{q})-\omega_{j_2}(-\mathbf{q})]$$
$$-\delta[\omega+\omega_{j_1}(\mathbf{q})+\omega_{j_2}(-\mathbf{q})]\}+2\{n[\omega_{j_2}(-\mathbf{q})]-n[\omega_{j_1}(\mathbf{q})]\}\delta[\omega-\omega_{j_1}(\mathbf{q})+\omega_{j_2}(-\mathbf{q})]). \quad (2)$$

Here, $\omega_j(\mathbf{q})$ is the DFPT calculated (zero temperature) frequency of the jth phonon mode at wave vector $\mathbf{q}$, and $n[\omega_j(\mathbf{q})]$, its thermal occupancy given by

$$n[\omega_j(\mathbf{q})]=\frac{1}{\exp\left[\frac{\hbar\omega_j(\mathbf{q})}{k_BT}\right]-1}. \quad (3)$$

The term $V^{(3)}(\mathbf{0},j;\mathbf{q},j_1;-\mathbf{q},j_2)$ in Eq. (2) represents the three-phonon coupling matrix elements.

The corresponding real part of the self-energy is then obtained by utilizing the Kramers-Kronig relation:

$$\Delta_j^{(3)}(\omega,T)=-\frac{1}{\pi}\mathcal{P}\int_{-\infty}^{\infty}d\omega'\frac{\Gamma^{(3)}(\omega',T)}{\omega'-\omega}, \quad (4)$$

where $\mathcal{P}$ stands for the principal value of the integral.

We note that the term in Eq. (2) involving $\delta[\omega+\omega_{j_1}(\mathbf{q})+\omega_{j_2}(-\mathbf{q})]$ does not contribute to $\Gamma_j^{(3)}(\omega,T)$ for positive ω. However, this term does need to be and is kept in our calculations of the real part of the phonon self-energy in Eq. (4).

Including the contributions from the cubic anharmonic effects treated only to the second order, the temperature dependence of the frequency of the jth mode at the center of the BZ is given by

$$\omega_j(T)=\omega_j(0)+\Delta_j^{0(\mathrm{qh})}+\Delta_j^{(\mathrm{qh})}(T)+\Delta_j^{(3)}(T). \quad (5)$$

The first term on the right-hand side of Eq. (5) is the DFPT calculated zero-temperature frequency of the jth phonon mode at the Γ point [obtained by evaluating $\omega_j(\mathbf{q})$ at $\mathbf{q}=0$]. The second term is the quasiharmonic contribution to the frequency shift at zero temperature due to the volume expansion induced by zero-point quantum fluctuations, whereas the third term is the quasiharmonic contribution due to the thermal expansion of the lattice. The fourth term corresponds to the cubic anharmonic contribution, given by $\Delta_j^{(3)}(T)=\Delta_j^{(3)}[\omega_j(0),T]$.

The quasiharmonic contribution comes from the temperature (or zero-point fluctuation) induced expansion/contraction of the lattice leading to a change in the second-order force constant matrix elements (or equivalently, the phonon frequencies) without changing the phonon population. It is straightforward to show that the T-dependent part can be expressed as

$$\Delta_j^{(\mathrm{qh})}(T)=\omega_j(0)\left\{\exp\left[-3\gamma_j\int_0^T\alpha(T')dT'\right]-1\right\}. \quad (6)$$

Here, $\gamma_j\equiv-\partial[\ln\omega_j(0)]/\partial(\ln V)$ (assumed to be temperature independent) is the Grüneisen parameter of a jth phonon mode, which describes the variations of the vibrational properties of a crystal lattice with respect to its volume. Also, $\alpha(T)$ is the linear thermal expansion coefficient [45] at temperature T, calculable as (a complete derivation is given in Appendix A of Ref. [46])

$$\alpha(T)=\frac{1}{3B}\sum_{\mathbf{q},j}\left(\left[-\frac{\partial\omega_j(\mathbf{q})}{\partial V}\right]\frac{\hbar^2\omega_j(\mathbf{q})}{k_BT^2}\times\frac{\exp[\hbar\omega_j(\mathbf{q})/k_BT]}{\{\exp[\hbar\omega_j(\mathbf{q})k_BT]-1\}^2}\right), \quad (7)$$

where B is the bulk modulus of the system.

In our calculations, the (otherwise singular) Cauchy principal value integrals and the sums involving Dirac-delta functions above were numerically evaluated using Lorentzian broadening, a widely used approximation [42,47,48], with a broadening parameter of 3 cm^{-1}.

VI. RESULTS AND DISCUSSION

A. Experimental results

The Raman spectra of YTO at 35 and 300 K are shown in Fig. 1. The assignment of the modes of pyrochlore YTO is done following Refs. [7,16]: P3 (308 cm^{-1}) as T_{2g}, P4 (324 cm^{-1}) as E_g, P5 (521 cm^{-1}) as A_{1g}, P6 (530 cm^{-1}) as T_{2g}, and P8 (709 cm^{-1}) as T_{2g}.

The additional low-frequency modes ∼100–200 cm^{-1} and the high-frequency modes ∼600–800 cm^{-1} are also observed in Refs. [7,9,16,37] and seen in pyrochlore YTO (see Fig. 1).

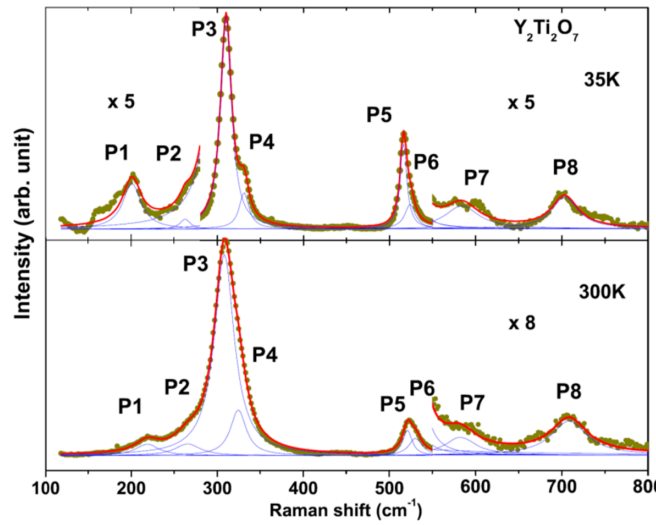

FIG. 1. Raman spectrum of $Y_2Ti_2O_7$ at 35 and 300 K. Closed circles represent the experimental data. The Raman intensity of the low-temperature spectrum for wave numbers <275 cm^{-1} has been rescaled for a better view. For the same reason, both the spectra are rescaled for wave numbers >550 cm^{-1}. The symmetry classifications assigned to the different modes labeled as P1–P8 are discussed in the text.

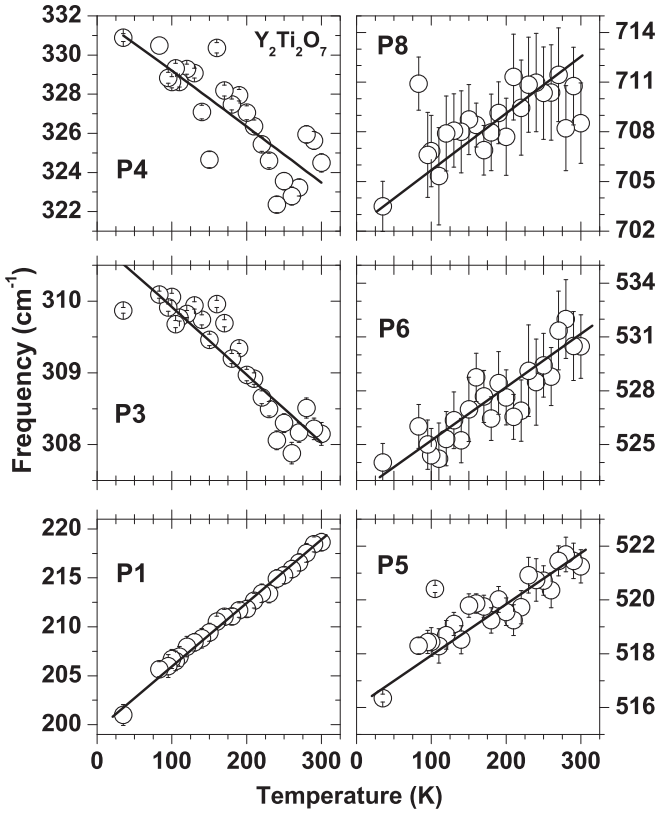

FIG. 2. Experimental results for the temperature dependence of the frequencies of modes P1, P3–P6, and P8 of nonmagnetic pyrochlore $Y_2Ti_2O_7$. Solid lines are guides to the eye.

The high-frequency modes can be assigned to second-order Raman processes [9]. We assign the low-frequency modes to IR active or silent modes rendered Raman active due to a possible lowering of the local symmetry at some crystallographic sites, as suggested in Ref. [37]. The remaining three modes are labeled as P1 (219 cm^{-1}), P2 (266 cm^{-1}), and P7 (583 cm^{-1}).

Figure 2 shows the temperature dependence of the frequencies of a few phonons of nonmagnetic pyrochlore YTO. Modes P1, P5, P6, and P8 show an anomalous temperature dependence, namely, their frequencies decrease on lowering the temperature. However, the frequencies of modes P3 and P4 have a normal temperature dependence. Data for P2 and P7 are not shown, as they are very weak.

B. Theoretical results

1. Harmonic phonon properties

The calculated values of the frequencies of all optical modes in YTO are shown in Table I. The results are compared with the current experimental values as well as other available data from the literature.

There have been earlier measurements and calculations of Raman active modes in YTO [49,52], with the lowest-frequency modes observed at ∼220 cm^{-1}. All Raman active modes in YTO involve vibrations of the oxygen atoms only, and our DFT calculations do not show any Raman active mode such as T_{2g} ∼220 cm^{-1}, in agreement with earlier results [49].

The modes closest in frequency in our calculations are two IR-active modes (T_{1u}), one ∼200 cm^{-1} and another ∼240 cm^{-1}, and one silent E_u mode at 181 cm^{-1}. These are normally Raman inactive but can appear in Raman spectra [7,10] due to displacive disorder at the Y and O′ sites in these systems. This displacive disorder leads to a relaxation of the selection rules [49], as a result of which IR modes can appear in Raman spectra and vice versa, and silent modes may become active and appear in Raman and IR spectra. Accordingly, for further discussions about self-energy corrections, temperature dependence, etc., we have included the above three (one silent and two IR active) modes and labeled them as M1, M2, and M3, as indicated in Table I, and assigned the M2 mode to the experimental P1 Raman mode. In the frequency range going up to 400 cm^{-1}, our DFT calculations predict a T_{2g} mode at ∼320 cm^{-1}, in reasonably good agreement with the present experimental value of 308 cm^{-1} and with the values available in the literature. The E_g mode is generally observed ∼330 cm^{-1} [8,9]. Our DFT value of 337 cm^{-1} for the E_g mode is in good agreement with our experimental value of 324 cm^{-1} and with the literature values. One each of the T_{2g} and A_{1g} modes of the pyrochlore titanates [52] is usually observed ∼450 and 510 cm^{-1}, respectively. Again, our calculated values of 453 and 508 cm^{-1} for the respective modes are in reasonably good agreement with the available literature values. However, in our Raman spectroscopic measurements, the theoretically predicted T_{2g} mode ∼450 cm^{-1} is not observed, which could be because its intensity is below the threshold, whereas the frequency for the A_{1g} mode is found to be 521 cm^{-1}, reasonably close to the theoretical value of 508 cm^{-1}. Among the two high-frequency Raman active modes with T_{2g} symmetry, one is calculated to be ∼581 cm^{-1}, whereas in the experiment, it is found to be ∼530 cm^{-1}. Our LDA value of the frequency of the highest-frequency Raman active mode is found to be ∼796 cm^{-1}, whereas it is observed to be ∼709 cm^{-1} in the present experiment. This observation is not in agreement with the other experimental values reported in Table I. It has been assigned as an overtone or combination of vibrational modes in the experimental measurements of Saha *et al.* [7] and in the lattice dynamical calculations by Gupta *et al.* [41] in titanates. Our calculated values are consistent with the calculations by Kumar *et al.* [49].

The calculated values of the frequencies of the IR active and silent modes in YTO pyrochlore are also shown in Table I. The results are again compared with the available literature data and are in reasonably good agreement with the available data for most of the modes. We label the calculated Raman active modes as well as two silent modes <800 cm^{-1} as M4–M10; the labels together with their correspondence with the observed modes (P1–P8) where possible are given in Table I. In the rest of this paper, we confine our discussions of the theoretical calculations to modes M1–M10.

The eigenvector displacement patterns for three low-frequency modes (M1–M3) and three high-frequency modes (M7, M8, and M10) are shown in Fig. 3. The eigenmode M1 involves the vibrations of only the Ti^{4+}, O^{2-}_{48f}, and O^{2-}_{8b} ions and not of Y^{3+}, whereas vibrations of all the ions contribute to the M2 and M3 modes. On the other hand, the high-frequency modes M7, M8, and M10 involve the vibrations of oxygen

TABLE I. Experimental and theoretical frequencies of optical phonon modes in pyrochlore $Y_2Ti_2O_7$, along with the available literature data. Modes with ⋆ indicate that they are experimentally observed but not found from the first-principles calculations. Frequencies with † denote modes that have not been assigned experimentally to any Raman active mode.

Modes	This paper (LDA)	This paper (Expt.)	Calc. [49]	Experimental
Raman				
$T_{2g}^{\star}$	–	–	–	225 [37]
T_{2g}	320 (M4)	308 (P3)	316	318 [37]
E_g	337 (M5)	324 (P4)	334	333 [37]
T_{2g}	453		449	450† [37]
A_{1g}	508 (M6)	521 (P5)	508	527 [37]
T_{2g}	581 (M8)	530 (P6)	582	531 [37]
T_{2g}	796 (M10)	709 (P8)	796	586 [37]
IR				
T_{1u}	79		74	105 [50]
T_{1u}	151		142	182 [2], 176 [50], 177 [51]
T_{1u}	197 (M2)	219 (P1)	189	248 [2], 248 [50], 245 [51]
T_{1u}	241 (M3)		238	299 [2], 285 [50], 293 [51]
T_{1u}	388		391	429 [2], 410 [50], 424 [51]
T_{1u}	465		456	460 [2], 462 [50], 467 [51]
T_{1u}	546		546	562 [2], 568 [50], 571 [51]
Silent				
T_{2u}	67		51	
T_{2u}	101		88	
E_u	115		106	
E_u	181 (M1)		171	
T_{1g}	260		270	
A_{2u}	303		300	
T_{2u}	313		301	
A_{2u}	393		393	
A_{2u}	409		408	
E_u	492		492	
T_{1g}	564 (M7)		572	
T_{2u}	601 (M9)		607	

atoms only, with the vibrations of O_{8b}^{2-} contributing only to the M8 mode and not at all to the M7 and M10 modes. In the case of the M8 mode, the amplitudes of vibration of the O_{8b}^{-2} ions are much larger than those of the O_{48f}^{-2} ions. In contrast, the M7 and M10 modes involve the vibrations only of O_{48f}^{-2} ions.

2. Anharmonic contributions to phonon properties

The mode Grüneisen parameter for the jth phonon mode at the center of BZ, defined by

$$\gamma_j \equiv -\frac{\partial \ln \omega_j(0)}{\partial \ln V} = -\frac{V}{\omega_j(0)}\frac{\partial \omega_j(0)}{\partial V}, \tag{8}$$

where V is the cell volume and $\omega_j(0)$ is the frequency of the jth phonon mode, was calculated as follows. Phonon frequencies were calculated at four different cell volumes (246.666, 244.399, 242.227, and 240.178 Å^3) by applying hydrostatic pressure to the system in the range of 0–6.0 GPa in steps of 2.0 GPa. Derivatives of the phonon frequencies with respect to volume at $V = 246.017$ Å^3 for the different phonon modes were calculated from the smooth functions for the frequencies as functions of volume obtained using cubic spline fittings. The calculated values of the mode Grüneisen parameters for the total of 10 vibrational modes M1–M10 between 180 and 800 cm^{-1} which are either IR or Raman active are given in Table II. There are no available data from the literature for the mode Grüneisen parameter for YTO to compare with our theoretical results. However, our calculated values are reasonably close to the experimentally obtained ones for a different

TABLE II. Calculated values of the mode Grüneisen parameters (γ) and FWHM. Theoretical results of the FWHM are also compared with the present experimental data. Here, $2\Gamma_j^{(3)}(35)$ implies the values of FWHM at $T = 35$ K.

	ω (cm^{-1})			$2\Gamma_j^{(3)}(35)$ (cm^{-1})	
Mode	Theory	Expt.	γ	Theory	Expt.
M1 (E_u)	181		1.82	5.4	
M2 (P1) (T_{1u})	197	219	2.73	5.7	25.8
M3 (T_{1u})	241		0.89	5.5	
M4 (P3) (T_{2g})	320	308	2.14	9.1	15.4
M5 (P4) (E_g)	337	324	1.89	9.3	13.7
M6 (P5) (A_{1g})	508	521	1.33	12.6	9.5
M7 (T_{1g})	564		1.73	31.2	
M8 (P6) (T_{2g})	581	530	1.34	9.8	14.7
M9 (T_{2u})	601		1.79	9.7	
M10 (P8) (T_{2g})	796	709	1.27	24.9	37.4

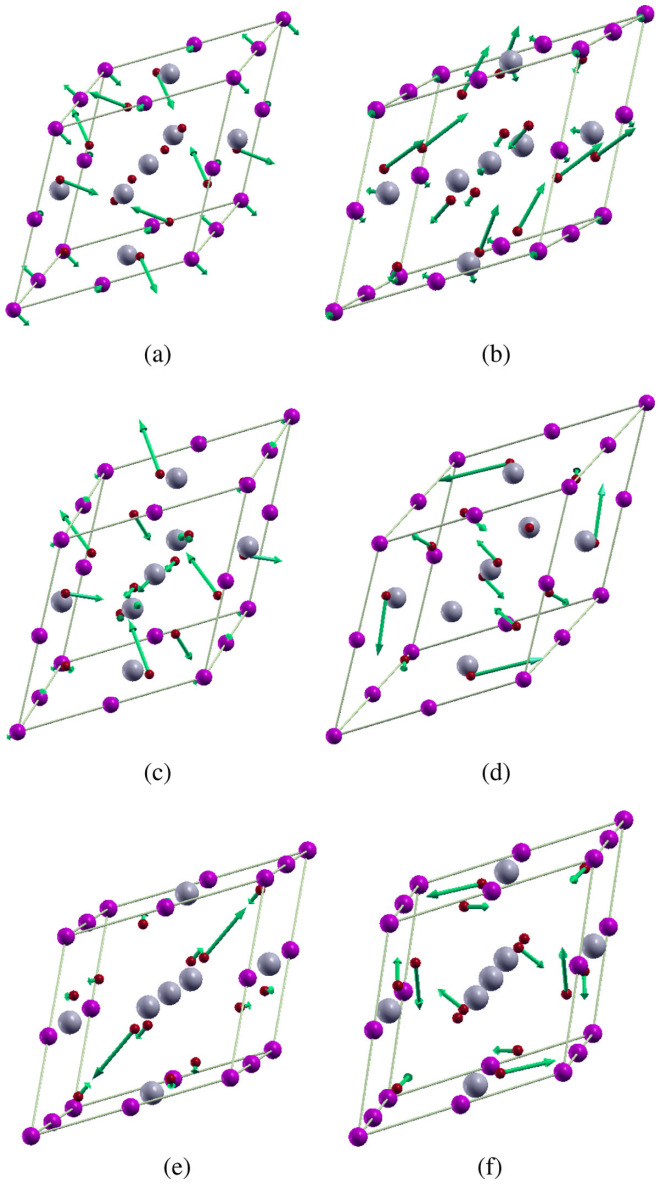

FIG. 3. Phonon eigenvector displacement of modes (a)–(c) M1–M3, (d) M7, (e) M8, and (f) M10. The large (gray), medium (pink), and small (red) spheres represent the Y, Ti, and O ions.

pyrochlore in the titanate family, namely, $Dy_2Ti_2O_7$ [53]. For example, our calculated values of the mode Grüneisen parameter in YTO for modes M1, M4, M6, and M10 are obtained as 1.8, 2.1, 1.3, and 1.3, respectively, whereas experimentally, in $Dy_2Ti_2O_7$ [53], they were obtained as 2.2, 1.7, 0.9, and 2.2, respectively.

Next, we discuss our calculations of $\alpha(T)$, the linear thermal expansion coefficient. The expression for it, given in Eq. (7), can be rewritten as

$$\alpha = \frac{1}{3BV}\sum_{\mathbf{q}j}\left(\gamma_j(\mathbf{q})\frac{[\hbar\omega_j(\mathbf{q})]^2}{k_B T^2}\frac{\exp\left[\hbar\omega_j(\mathbf{q})/k_B T\right]}{\{\exp\left[\hbar\omega_j(\mathbf{q})/k_B T\right]-1\}^2}\right), \tag{9}$$

where $\gamma_j(\mathbf{q})$ is the wave-vector-dependent mode Grüneisen parameter for the jth mode.

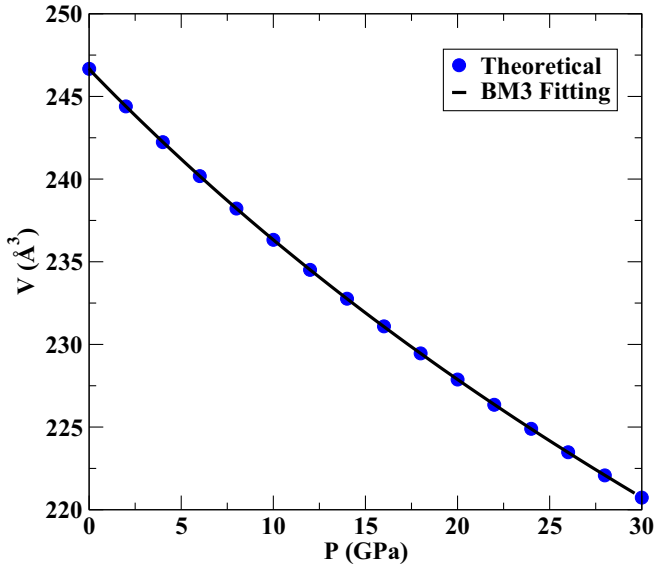

FIG. 4. Calculated values of the primitive unit-cell volume as a function of pressure. The solid line represents the fitted values using the third-order Birch-Murnaghan equation of state. The bulk modulus and its pressure derivative are obtained as 214 GPa and 4.2, respectively.

As can be seen from Eq. (9), the calculation of $\alpha(T)$ requires as inputs the bulk modulus as well as the $\gamma_j(\mathbf{q})$. These are respectively obtained using nonlinear fittings to the volume vs pressure and the $\omega_j(\mathbf{q})$ vs volume data. We have obtained the bulk modulus of YTO by fitting the calculated volume vs pressure data (see Fig. 4) to the third-order Birch-Murnaghan equation of state [54]. Our calculated value of the bulk modulus of 214 GPa is reasonably close to the experimentally obtained value of 204 GPa [55] and in agreement with earlier theoretical values of 229 GPa [56] and 205 GPa [57].

Using Eq. (9), we have calculated the linear thermal expansion coefficient $\alpha(T)$. Here, we used a $30 \times 30 \times 30$ **q**-grid to evaluate the sum over the wave vectors in Eq. (9). The symmetry of the face-centered space group was used to generate the different **q**-points in the BZ, which in our case numbered 751. The results are shown in Fig. 5. There is no data available in the literature for the temperature dependence of $\alpha(T)$ for YTO for us to compare with. However, our calculated value of 11.2×10^{-6} K^{-1} for the linear thermal expansion coefficient at 300 K is in reasonably good agreement with the experimentally measured value of 10.6×10^{-6} K^{-1} at 293 K by Farmet *et al.* [58] and of 8.36×10^{-6} K^{-1} by Gill *et al.* [59] and in excellent agreement with the theoretically calculated value of 11×10^{-6} K^{-1} by Matsumoto *et al.* [60] using a first-principles molecular dynamics study.

The calculated values of the temperature-dependent quasiharmonic shifts in the frequencies of the optical modes of YTO obtained using the above results and Eq. (6) are shown in Fig. 6. We note that $\Delta_j^{(\mathrm{qh})}(T)$ decrease with increasing temperature for all M1–M10 modes, and the maximum change is ∼6.5, 6.7, and 7.0 cm^{-1} for modes M7, M10, and M9, respectively. Hence, at the level of including only the quasiharmonic contributions, all the phonon modes would show

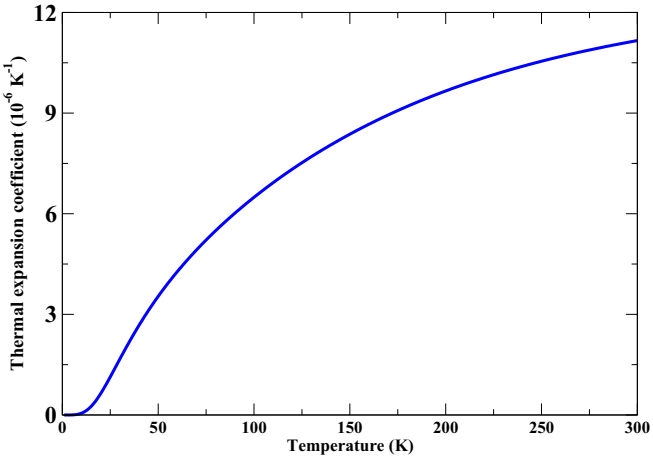

FIG. 5. Theoretical results of the temperature dependence of linear thermal expansion coefficient.

normal behavior, i.e., softening, or redshifting as the temperature increases.

Next, within the approximations mentioned earlier for the computation of the phonon self-energies, values of the full width at half maximum (FWHM) or $2\Gamma_j^{(3)}(T) = 2\Gamma_j^{(3)}[\omega_j(0), T]$ evaluated at $T = 35$ K are provided in Table II. Since the experimental results also include an instrumental broadening in the results, the calculated widths were increased by 5 cm^{-1} to compare with the experimental data. A comparison of our experimental and theoretical results for the FWHM as a function of temperature for some of the phonon modes is shown in Fig. 7. Linear-in-T fits to the experimental data are also shown as guides to the eye. We note

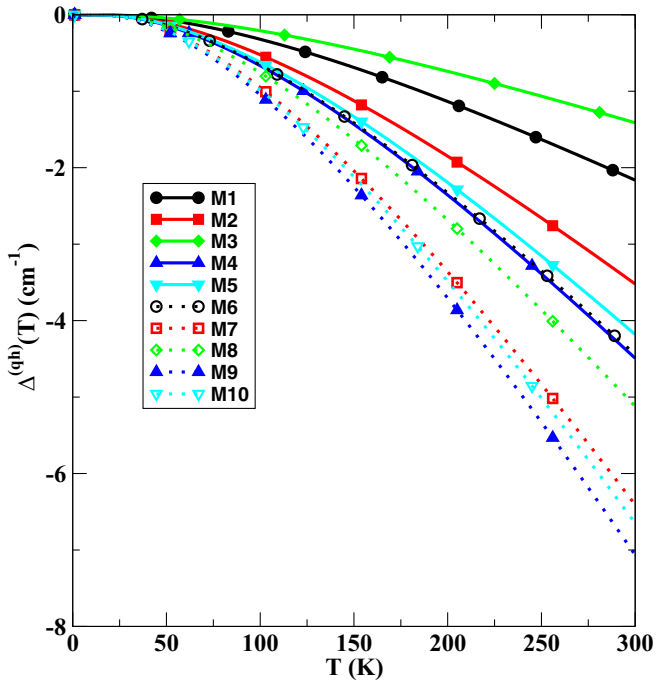

FIG. 6. Theoretical results for the temperature dependence of quasiharmonic contributions for modes M1–M10 in $Y_2Ti_2O_7$.

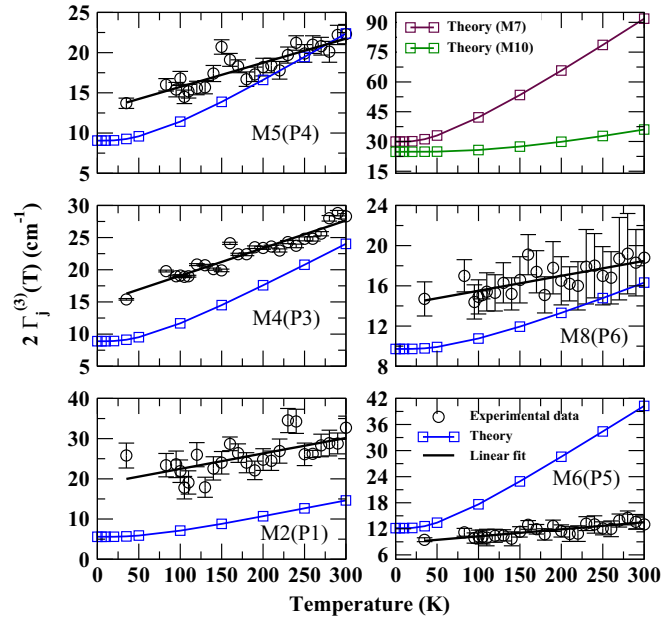

FIG. 7. Comparison of the experimental and theoretical values of the full width at half maximum (FWHM) as a function of temperature.

that the experimental results are for the temperature range of 35–300 K, whereas the theoretical calculations are over the range from 0–300 K. The experimental FWHM for mode P1 is ∼25.8 cm^{-1} at 35 K and changes to 32.7 cm^{-1} at 300 K, an increase of 6.9 cm^{-1}, whereas the theoretical values of the FWHM for this mode (denoted as M2) changes from 5.7 cm^{-1} at 35 K to 14.6 cm^{-1} at 300 K, an increase of 8.7 cm^{-1}. While the theoretical value of the FWHM at 35 K is less than the experimental value, the increase over the range of 35–300 K is comparable. We find roughly similar features in the case of the theoretically computed modes M4, M5, and M8, corresponding to the experimental modes P3, P4, and P6 respectively; the theoretical results for the FWHM are smaller than the experimental ones, but the rates of increase with temperature are comparable. On the other hand, the theoretical FWHM for mode M6 is larger than the measured FWHM of the corresponding mode P5 at 35 K and in addition shows a much larger rate of increase with increasing temperature.

The theoretically calculated values of the FWHM as a function of temperature for the two high-frequency modes, namely, the M7 (optically silent) and M10 (Raman active) modes, are also shown in Fig. 7 (top right panel). The zero-temperature values of the FWHM for both these modes, especially for mode M7, are larger than those for all the other modes. Another noteworthy feature is that, compared with the other modes, the FWHM for the M7 mode shows a much larger increase of ∼60 cm^{-1} as the temperature increases from 0 to 300 K. The large values of the FWHM for these modes may be connected with the anomalous temperature dependence of their frequencies discussed below.

The cubic anharmonic shifts $\Delta_j^{(3)}(T)$ for modes M1–M10 are shown in Fig. 8. The shifts for M1–M6 and M9 show negative contributions of increasing magnitude with increasing temperature; this will cause these phonons to soften with

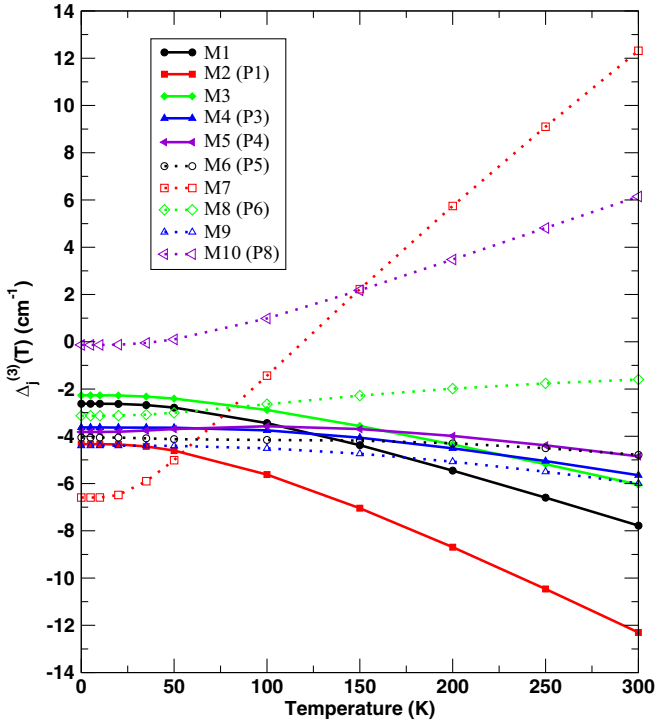

FIG. 8. Theoretical results of the temperature dependence of cubic anharmonic contributions to the frequencies of the phonon modes in $Y_2Ti_2O_7$.

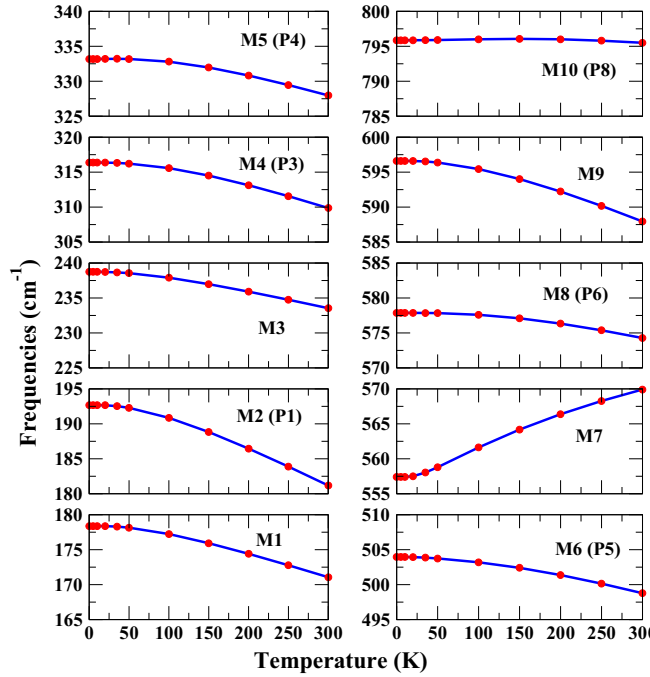

FIG. 9. Theoretical results of the temperature dependence of the frequencies of several phonon modes in $Y_2Ti_2O_7$.

increasing temperature, which is the normal behavior expected for phonons in any system. On the other hand, modes M7, M8, and M10 behave differently: with increasing temperature, the shifts for M8 are negative but of decreasing magnitude, whereas M7 and M10 have positive shifts of increasing magnitude (although M7 starts out being negative at low T). These changes correspond to hardening or blue shifts with increasing temperature. This anomalous trend is like the trends observed experimentally for the Raman modes P5, P6, P8, and P1.

However, the overall temperature dependence of the frequency of any phonon mode also has contributions from the quasiharmonic shift, which we recall corresponds only to softening with increasing temperature. When we add all the contributions, i.e., the quasiharmonic as well as the cubic anharmonic shifts to the zero-temperature frequencies (see Fig. 9), we find that almost all the modes behave normally (i.e., their frequencies decrease with increasing temperature), except for the M7 and M10 modes, which show anomalous behavior (i.e., their frequencies increase with increasing temperature). Among the two anomalous modes, M7 shows a much bigger anomaly [$\omega(300\ \mathrm{K}) - \omega(0\ \mathrm{K}) = 12\ \mathrm{cm}^{-1}$] than M10, but it is a silent mode. The M10 mode frequency has an interesting nonmonotonicity with increasing temperature—its frequency first increases up to ∼150 K, then it starts decreasing, but the changes are much too small to be able to explain the changes observed experimentally for the P8 mode with which it is identified. We note that we have obtained theoretical results for the temperature dependence of the frequencies, FWHM, etc., of all the other modes in YTO, but these are not shown or discussed here. None of those modes show any anomalies. For details, see Ref. [46].

While our theoretical calculations show that phonon self-energy contributions arising from anharmonic interactions can indeed lead to an anomalous temperature dependence of the phonon frequencies, the details are not in agreement with experiments. The theoretically calculated anomalies appear only for the two high-frequency modes, namely, M7 and M10, as seen in their relatively large FWHM and their anomalous softening with decreasing temperature. The M7 mode does not show up in the experiment, as it is optically silent, and the observed changes for the P8 mode are much larger (10 cm^{-1} change from 35 to 300 K) than the calculated changes for the M10 mode to which it corresponds (0.2 cm^{-1} increase from 0 to 150 K, followed by 0.6 cm^{-1} decrease from 150 to 300 K). The theory fails to explain the anomalies observed in the experiments (see Sec. VI A) for the low-frequency (P1) or the intermediate-frequency (P5, P6) modes.

We note that, as discussed earlier (see Fig. 3 and the related discussion), the two theoretically anomalous modes M7 and M10 involve vibrations only of the O_{48f}^{-2} ions. This raises the possibility that their anomalous nature may be connected with the displacements of the O_{48f}^{-2} ions. The reason behind the anomalous nature of the P1 mode ∼200 cm^{-1}, observed in experiments (see Fig. 2) but not in our theoretical calculations, is not clear. In Refs. [7,16], it has been suggested that the vibrations of Ti^{4+} ions are responsible for the anomalous nature of this mode. In our theoretical calculations, the eigenvector displacement patterns of the M1–M3 modes (see Fig. 3) involve vibrations of Ti^{4+} ions but along with substantial contributions from the vibrations of the oxygen atoms. However, all three modes behave normally (blueshift with cooling) as functions of temperature. Clearly, cubic anharmonic

TABLE III. Comparison of the theoretical values of the phonon frequencies calculated at $T = 0$ K with and without the anharmonic corrections due to quantum fluctuations. We also compare the calculated values at $T = 35$ K with the corresponding experimental values. In the last column, we provide the frequency change due to quantum fluctuations at $T = 0$ K within the quasiharmonic approximation, denoted by $\Delta_j^{0(\mathrm{qh})}$. $\omega_j(0)$ corresponds to the LDA value of the frequency of jth mode calculated at $T = 0$ K. All of $\omega_j(0)$, $\Delta_j^{(\mathrm{qh})}(T)$, $\Delta_j^{(3)}(T)$, and $\Delta_j^{0(\mathrm{qh})}$ are in units of cm^{-1}. (For notational simplicity, we do not include K in the temperature values which are arguments of these functions.)

Mode	$\omega_j(0)$	$\omega_j(0)$ $+\Delta_j^{(3)}(0)$	$\omega_j(0)+\Delta_j^{(\mathrm{qh})}(35)$ $+\Delta_j^{(3)}(35)$	$\omega^{\mathrm{Expt}}(35)$	$\Delta_j^{0(\mathrm{qh})}$
M1	181	178.4	178.3		−2.9
M2 (P1)	197	192.7	192.5	201	−4.8
M3	241	238.7	238.7		−1.9
M4 (P3)	320	316.4	316.3	309.9	−6.1
M5 (P4)	337	333.2	333.2	330.9	−5.6
M6 (P5)	508	504	503.9	516.4	−6.0
M7	564	557.4	558		−8.6
M8 (P6)	581	577.9	577.9	524	−6.9
M9	601	596.6	596.5		−9.5
M10 (P8)	796	795.9	795.9	703.5	−9.0

phonon-phonon interactions treated up to the second order cannot explain the experimentally observed anomalous behavior of the low- or intermediate-frequency phonons. We further note that it is quite important to understand the frequency dependence of phonon linewidths and line shifts, which we present in Appendix A.

C. Additional comments on the comparison between experimental and theoretical results for phonon frequencies and linewidths

As briefly mentioned earlier, zero-point quantum fluctuations can induce a change in the cell volume relative to its value as calculated from DFT even at $T = 0$ K. We have calculated this change in the cell volume of YTO (including its temperature dependence) using the Debye model, as implemented in the GIBBS2 code [61]. The resulting change at $T = 0$ K is $\Delta V = 2.184$ Å^3. This leads, via the Grüneisen constant, to an additional temperature-independent component of the quasiharmonic corrections to the phonon frequencies, which we denoted as $\Delta_j^{0(\mathrm{qh})}$ in Eq. (5). These corrections are relatively small (typically <1%) and are listed in Table III but have not been included in any of the figures related to the temperature-dependent phonon properties. The temperature-dependent components of the quasiharmonic shifts, which vanish at $T = 0$ K [see Eq. (9)], were already included in the results presented and discussed earlier.

We note that quantum fluctuations are also responsible for the fact that the third-order contributions to the linewidths and line shifts are nonzero even at zero temperature (see Figs. 7 and 8). We have also shown in Table III the numerical values of the phonon frequencies that include these corrections at 0 K as well as at 35 K, the lowest temperature reached in our experiments, together with the corresponding experimental values at 35 K. From Table III, it is clear that with the inclusion of $\Delta_j^{0(\mathrm{qh})}$ the agreement between theoretical and experimental frequencies at 35 K improves for some of the modes [especially M4 (P3) and M5 (P4)] but worsens for others.

TABLE IV. A comparison of the experimental and theoretical values of the frequencies calculated at $T = 35$ and 300 K. Here, we also provide a difference in frequencies as $\Delta\omega = \omega(300) - \omega(35)$. The units of frequencies and their differences are in cm^{-1}. (For notational simplicity, we do not include K in the temperature values which are arguments of these functions.)

	Theoretical			Experimental		
Mode	$\omega(35)$	$\omega(300)$	$\Delta\omega$	$\omega(35)$	$\omega(300)$	$\Delta\omega$
M1	178.3	171	−7.3			
M2 (P1)	192.5	181.2	−11.3	201	218.7	17.7
M3	238.7	233.5	−5.2			
M4 (P3)	316.3	309.9	−6.4	309.9	308.2	−1.7
M5 (P4)	333.2	328	−5.2	330.9	324.5	−6.4
M6 (P5)	503.9	498.8	−5.1	516.4	521.3	4.9
M7	558	569.9	11.9			
M8 (P6)	577.9	574.3	−3.6	524	530.5	6.5
M9	596.5	587.9	−8.6			
M10 (P8)	795.9	795.5	−0.4	703.5	708.5	5

Furthermore, in Tables IV and V, we have provided a comparison of the experimental and theoretical frequencies and the linewidths (FWHM) at $T = 35$ and 300 K as well as their differences. As discussed earlier in the paper, theoretically, we have been unable to capture the observed phonon anomalies. As regards line shifts, the best qualitative agreement is with the normal behavior observed for the P3 and P4 modes, with the agreement being even quantitatively reasonable in the case of the latter.

Next, the FWHM calculated at $T = 35$ and 300 K and their differences $\{\Delta[2\Gamma_j^{(3)}] = 2\Gamma_j^{(3)}(300) - 2\Gamma_j^{(3)}(35)\}$are compared with the respective observed values in Table V. As regards the linewidths, except for mode M6 (P5), the theoretical values of $\Delta[2\Gamma_j^{(3)}]$ are comparable with the observed values for most of the modes. We also note that mode M7 has an anomalously large value of $\Delta[2\Gamma_j^{(3)}] = 60.7$ cm^{-1}. This behavior of mode M7 is likely connected with the anomalous behavior of its frequency as a function of temperature.

VII. CONCLUSIONS

In conclusion, in this paper, we have presented studies on the temperature dependence of the properties of phonons in the pyrochlore compound YTO using Raman spectroscopy measurements as well as theoretical calculations based on first-principles DFT. In the experiments, we observe an anomalous softening of four of the phonon modes with decreasing temperature. The maximum anomaly is seen in a mode ∼200 cm^{-1}. Our first-principles calculations using quasiharmonic and cubic-anharmonic effects treated to the leading (second) order also find an anomalous temperature dependence of the phonon frequencies in this system but only for two high-frequency modes, namely, T_{1g} (M7 mode, at

TABLE V. A comparison of the experimental and theoretical values of the FWHM at $T = 35$ and 300 K. Here, we also provide the temperature-induced difference in the FWHM. $\Delta(2\Gamma) = 2\Gamma(300) - 2\Gamma(35)$. The units of FWHM and their differences are in cm^{-1}. (For notational simplicity, we do not include K in the temperature values which are arguments of these functions.)

	Theoretical			Experimental		
Mode	$2\Gamma_j^{(3)}(35)$	$2\Gamma_j^{(3)}(300)$	$\Delta[2\Gamma_j^{(3)}]$	$2\Gamma_j^{(3)}(35)$	$2\Gamma_j^{(3)}(300)$	$\Delta[2\Gamma_j^{(3)}]$
M1	5.4	10.5	5.1			
M2 (P1)	5.7	14.6	8.9	25.8	32.7	6.9
M3	5.5	10.3	4.8			
M4 (P3)	9.1	24.0	14.9	15.4	28.3	12.9
M5 (P4)	9.3	22.4	13.1	13.7	22.3	8.6
M6 (P5)	12.6	40.3	27.7	9.5	13	3.5
M7	31.2	91.9	60.7			
M8 (P6)	9.8	16.3	6.5	14.7	18.8	4.1
M9	9.7	17.1	7.4			
M10 (P8)	24.9	36.0	11.2	37.4	50.4	13

564 cm^{-1}) and T_{2g} (M10 mode, at 796 cm^{-1}). The M7 mode has the larger shifts but is optically silent. The M10 mode, identifiable with the highest-frequency experimental mode (P8), behaves interestingly in that its frequency first hardens with increasing temperature up to 150 K and then softens due to the competition between the hardening contribution from cubic anharmonicity and the softening contribution from quasiharmonic shifts, but the changes are small. In contrast, as shown in Fig. 2, experimentally, the P8 mode shows a clear anomalous hardening with increasing temperature, and the changes are more than an order of magnitude larger. Furthermore, the theoretical calculations fail to capture the anomalous behavior of the low- or intermediate-frequency modes.

Nonetheless, the work we have presented here suggests that strong anharmonic phonon-phonon interactions are indeed the likely cause of the observed phonon anomalies in the titanate pyrochlores, as also of the observed and anticipated anomalies in spin-ice $Dy_2Ti_2O_7$ and nonmagnetic $Lu_2Ti_2O_7$ [7]. It is also plausible that the strong anharmonic interactions are connected with the vacant 8*a* sites at the center of Ti^{4+} tetrahedra and the large vibrations of the O_{48f} ions. However, in this paper, we also make clear that a detailed explanation of the anomalies, especially for the low- and intermediate-frequency modes, poses an open, interesting, and challenging theoretical problem, requiring the inclusion of effects due to anharmonic interactions higher than cubic anharmonicity (see Appendix B for some comments on the effects of quartic anharmonic interactions) and perhaps a nonperturbative treatment of such interactions.

ACKNOWLEDGMENTS

P.K.V. is thankful to the Council of Scientific and Industrial Research, India and the Department of Science and Technology (DST), India, for financial support. The calculations were performed using the Cray XC40 at the Supercomputer Education and Research Centre at IISc. H.R.K. gratefully acknowledges support from the Science and Engineering Research Board of the DST, India, under Grant No. SB/DF/005/2017. A.K.S. thanks DST for the Year of Science Professorship for financial support.

APPENDIX A: FREQUENCY DEPENDENCE OF LINE SHIFTS AND LINEWIDTHS, TWO-PHONON DENSITY OF STATES, AND KINEMATICAL FUNCTION

It would be interesting to know the frequency dependence of the linewidth and line-shift functions defined in Eqs. (2) and (4). Unfortunately, the D3Q code we use for computing $\Gamma_j^{(3)}$ and $\Delta_j^{(3)}$ gives out their values only at the jth unperturbed phonon frequency and not at arbitrary values of ω. The best one can do under the circumstances is to plot their values for all the modes, which is equivalent to sampling each of them at different single frequencies on a nonuniform grid of ω. These are shown in Figs. 10 and 11 together with smooth interpolations shown as dotted curves to serve as guides to

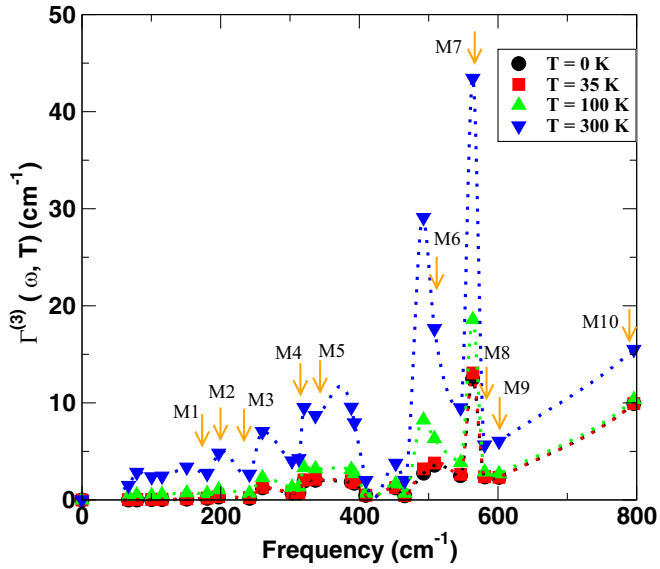

FIG. 10. Frequency dependence of the collective phonon linewidth function $\Gamma^{(3)}(\omega, T)$ defined in the text calculated at four different temperatures. The positions of modes M1–M10 are marked by arrows. Note that $\Gamma^{(3)}(\omega, T)$ for $T = 0$ and 35 K are almost the same. The interpolated functions shown as dotted curves are meant only to serve as guides to the eye; there are no actual data points at frequencies other than the points marked by the symbols.

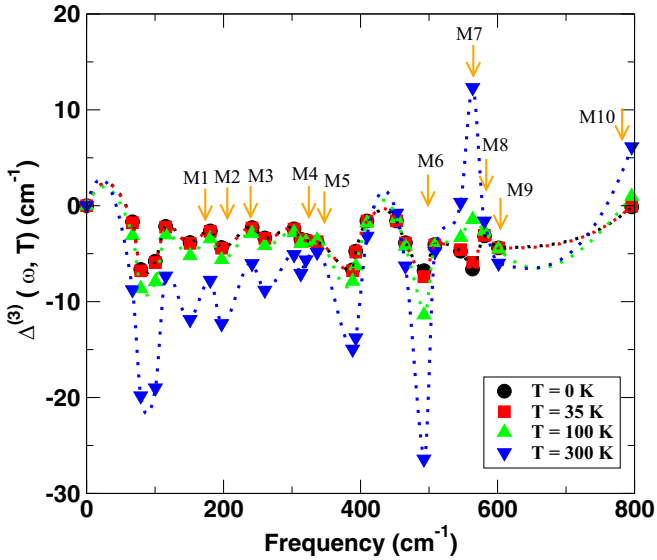

FIG. 11. Frequency dependence of the collective phonon line-shift function $\Delta^{(3)}(\omega, T)$ defined in the text calculated at four different temperatures. The positions of modes M1–M10 are marked by arrows. Note that $\Delta^{(3)}(\omega, T)$ for $T = 0$ and 35 K are almost the same. The interpolated functions shown as dotted curves are meant only to serve as guides to the eye; there are no actual data points at frequencies other than the points marked by the symbols.

the eye. For convenience, we will refer to these collective interpolated functions as $\Gamma^{(3)}(\omega, T)$ and $\Delta^{(3)}(\omega, T)$.

We emphasize that these collective linewidth and line-shift functions may not correspond to any of the j-dependent linewidth and line-shift functions. Nevertheless, if we assume that the many, rather sharp peaks and troughs seen in them are also features shared by the j-dependent linewidth and line-shift functions, it is clear that the phonon linewidths and the line shifts will depend sensitively on the frequencies at which the j-dependent linewidth and line-shift functions are evaluated. One might wonder whether one can make clever, perhaps self-consistent, choices for these frequencies that could lead to better correspondence with experiments. Needless to say, the only systematic prescription is for the evaluation to be done at $\omega_j(0)$, the unperturbed phonon frequencies evaluated using DFT, as we have done. Any other prescription, such as evaluating the functions at phonon frequencies that include the quasiharmonic corrections (which in themselves arise from anharmonic interactions relative to a reference unit-cell volume), for example, or self-consistently, will not be systematic in the inclusion of the anharmonic effects.

Furthermore, Fig. 11 suggests that it is unlikely that even such prescriptions can generate line shifts with anomalous temperature dependence for any of the low-frequency phonon modes, for the line-shift function in this figure has substantial positive values that increase with increasing temperature and are large enough to overcome the negative quasiharmonic corrections only in the high-frequency range, essentially only for mode M7 which lies near its peak, as we have shown.

One can gain some additional insights into the relative importance of the contributions arising from the matrix elements vs the rest of the terms in Eq. (2) by replacing the matrix elements with a constant, which we will denote as $V^{(3)}$. This causes the linewidth functions in Eq. (2) to become j independent and proportional to what is called the two-phonon density of states (TDOS) [62], which we denote as $D^{(2)}(\omega, T)$, given by

$$D^{(2)}(\omega, T) = \frac{1}{N} \sum_{\mathbf{q}, j_1, j_2} (\{n[\omega_{j_1}(\mathbf{q})] + n[\omega_{j_2}(-\mathbf{q})] + 1\}\{\delta[\omega - \omega_{j_1}(\mathbf{q}) - \omega_{j_2}(-\mathbf{q})] - \delta[\omega + \omega_{j_1}(\mathbf{q}) + \omega_{j_2}(-\mathbf{q})]\}$$
$$+ 2\{n[\omega_{j_2}(-\mathbf{q})] - n[\omega_{j_1}(\mathbf{q})]\}\delta[\omega - \omega_{j_1}(\mathbf{q}) + \omega_{j_2}(-\mathbf{q})]). \tag{A1}$$

The first and second set of terms in the curly brackets are commonly referred to as down- and up-conversion phonon processes, respectively. As in the case of $\Gamma_j^{(3)}(\omega, T)$, the $\delta[\omega + \omega_{j_1}(\mathbf{q}) + \omega_{j_2}(-\mathbf{q})]$ term contributes only when ω is negative.

Within the same approximation, the line-shift functions are also j independent and are proportional to what is called the two-phonon kinematical function, which we denote as $P^{(2)}(\omega, T)$. This function is just the Hilbert transform of $D^{(2)}(\omega, T)$ and is given by

$$P^{(2)}(\omega, T) = \frac{1}{N} \sum_{\mathbf{q}, j_1, j_2} \mathcal{P}\left\{ \frac{n[\omega_{j_1}(\mathbf{q})] + n[\omega_{j_2}(-\mathbf{q})] + 1}{\omega - \omega_{j_1}(\mathbf{q}) - \omega_{j_2}(-\mathbf{q})} - \frac{n[\omega_{j_1}(\mathbf{q})] + n[\omega_{j_2}(-\mathbf{q})] + 1}{\omega + \omega_{j_1}(\mathbf{q}) + \omega_{j_2}(-\mathbf{q})} + 2\frac{n[\omega_{j_2}(-\mathbf{q})] - n[\omega_{j_1}(\mathbf{q})]}{\omega - \omega_{j_1}(\mathbf{q}) + \omega_{j_2}(-\mathbf{q})} \right\}, \tag{A2}$$

where $\mathcal{P}$ denotes the Cauchy principal part. As earlier, the temperature dependence of $D^{(2)}(\omega, T)$ and $P^{(2)}(\omega, T)$ arises via the phonon occupancy factors n.

Figure 12 shows the TDOS calculated at $T = 0$, 35, 100, and 300 K. The DFT-calculated frequencies of phonon modes M1–M10 are also marked in the plot. To get additional insights, we have plotted in Fig. 13 the separate contributions coming from the up- and down-conversion processes in $D^{(2)}(\omega, T)$ for the same four temperatures. At any temperature, at high frequencies, the contributions from up-conversion are significantly smaller than those from down-conversion, as there are fewer channels available for the former. In contrast, for the down-conversion process, there is a wide frequency window with a significantly large TDOS. While there is a rough correspondence between the relatively larger values of TDOS of the higher-frequency modes with their relatively

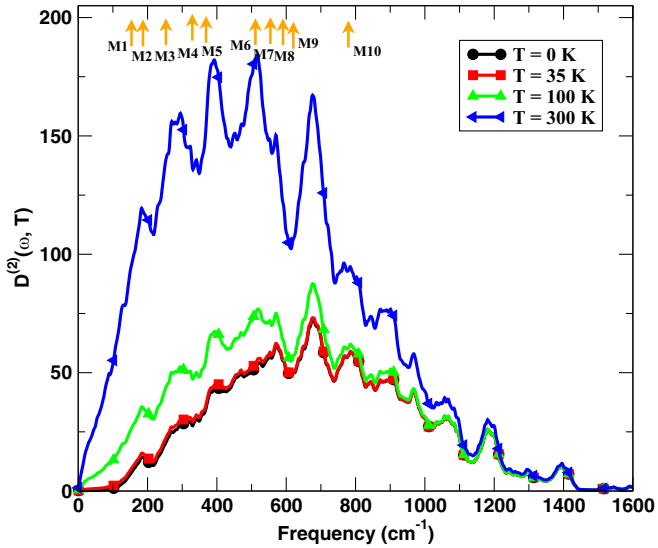

FIG. 12. Two-phonon density of states of $Y_2Ti_2O_7$ calculated at four different temperatures. Modes M1–M10 are also marked by arrows. We note that the $D^{(2)}(\omega, T)$ values at $T = 0$ and 35 K are almost the same.

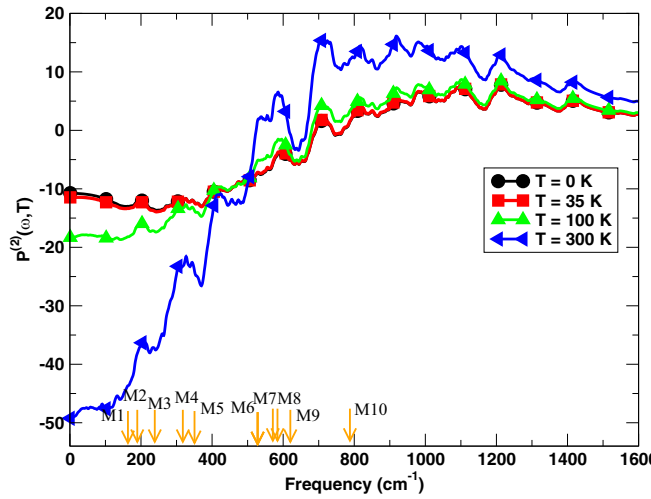

FIG. 14. Frequency dependence of the two-phonon kinematical function $P^{(2)}(\omega, T)$ of $Y_2Ti_2O_7$ calculated at four different temperatures. For clarity, modes M1–M10 are also marked by arrows. We note here that the values of $P^{(2)}(\omega, T)$ calculated at $T = 0$ and 35 K are almost the same.

larger linewidths, the correspondence is not one to one. In the frequency region between modes M9 and M10, $D^{(2)}(\omega, T)$ decreases with increasing frequency, whereas $\Gamma^{(3)}(\omega, T)$ increases.

Next, the frequency dependence of the two-phonon kinematical function $P^{(2)}(\omega, T)$ calculated at four different temperatures is shown in Fig. 14. It looks qualitatively like

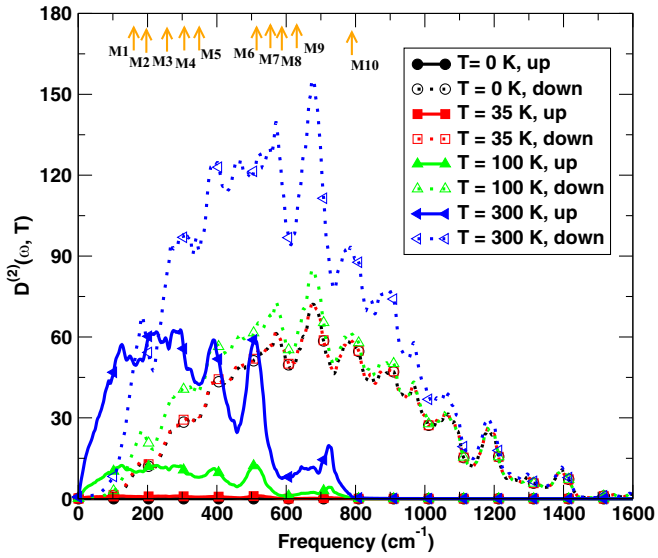

FIG. 13. The contribution of the up- and down-conversion decay processes to the two-phonon density of states of $Y_2Ti_2O_7$ calculated at four different temperatures. Modes M1–M10 are also marked by arrows. We, again, note that the up-conversion contribution to $D^{(2)}(\omega, T)$ is almost negligible at $T = 0$ and 35 K, whereas the down-conversion contributions are almost the same at these two temperatures.

$\Delta^{(3)}(\omega, T)$ in that it is negative in the low-frequency region but positive at high frequencies. However, quantitatively, it differs substantially from $\Delta^{(3)}(\omega, T)$, with fewer less sharp peaks.

The differences we have pointed out above between $D^{(2)}(\omega, T)$ and $\Gamma^{(3)}(\omega, T)$, and even more so between $P^{(2)}(\omega, T)$ and $\Delta^{(3)}(\omega, T)$, suggest that matrix elements of the anharmonic interactions play an important role in determining the temperature dependence of the phonon linewidths and line shifts.

We note that all the curves shown in Figs. 12–14 are based on calculations done at very many more points than those corresponding to the different symbols shown in these figures. The latter have been shown merely to help readers to distinguish between the different curves in the print version of this paper.

APPENDIX B: QUARTIC ANHARMONIC EFFECTS

In this paper, we have so far not included quartic anharmonic effects in our calculations. However, it is interesting to ask whether line shifts including these effects could help to explain the anomalous temperature dependence of the line shifts seen experimentally. Below, we provide a brief discussion of the expressions for the phonon linewidths and line shifts arising from quartic anharmonic interactions treated up to the second order as well as a discussion of their temperature dependence within the framework of the simplifying assumption that the four-phonon coupling constants are independent of their arguments. A full calculation, which requires an *ab initio* calculation of the four-phonon coupling matrix elements using DFPT, is extremely challenging and beyond the scope of this paper.

The quartic anharmonic contributions to the line-shift functions up to and including the four-phonon couplings $V^{(4)}$ treated to the second order are given by [63,64]

$$\Delta_j^{(4a)}(\omega,T)=\frac{24}{\hbar}\sum_{\mathbf{q}_1,j_1}V(\mathbf{0},j;\mathbf{0},j;\mathbf{q}_1,j_1;-\mathbf{q}_1,j_1)\left(n_1+\frac{1}{2}\right), \tag{B1}$$

$$\begin{aligned}\Delta_j^{(4b)}(\omega,T)=&\frac{-96}{\hbar^2}\sum_{\mathbf{q}_1,j_1}\sum_{\mathbf{q}_2,j_2}\sum_{\mathbf{q}_3,j_3}|V(\mathbf{0},j;\mathbf{q}_1,j_1;\mathbf{q}_2,j_2;\mathbf{q}_3,j_3)|^2\\&\times\mathcal{P}\Bigg\{[(n_1+1)(n_2+1)(n_3+1)-n_1n_2n_3]\left(\frac{1}{\omega+\omega_1+\omega_2+\omega_3}-\frac{1}{\omega-\omega_1-\omega_2-\omega_3}\right)\\&+3[n_1(n_2+1)(n_3+1)-(n_1+2)n_2n_3]\left(\frac{1}{\omega-\omega_1+\omega_2+\omega_3}-\frac{1}{\omega+\omega_1-\omega_2-\omega_3}\right)\Bigg\},\end{aligned} \tag{B2}$$

$$\begin{aligned}\Delta_j^{(4c)}(\omega,T)=&\frac{-576}{\hbar^2}\sum_{\mathbf{q}_1,j_1}\sum_{j_2}\sum_{\mathbf{q}_3,j_3}V(\mathbf{0},j;\mathbf{0},j;-\mathbf{q}_1,j_1;\mathbf{q}_1,j_2)V(\mathbf{q}_1,j_1;-\mathbf{q}_1,j_2;\mathbf{q}_3,j_3;-\mathbf{q}_3,j_3)\\&\times\mathcal{P}\left(\frac{n_1+n_2+1}{\omega_1+\omega_2}-\frac{n_1-n_2}{\omega_1-\omega_2}\right)\left(n_3+\frac{1}{2}\right).\end{aligned} \tag{B3}$$

where $\mathcal{P}$ denotes the principal value.

Of these, $\Delta_j^{(4a)}$ and $\Delta_j^{(4c)}$ correspond to first- and second-order Hartree contributions to the self-energy of the phonons, have no frequency dependence, and hence only contribute to the line shifts. The linewidth function to the second order in the quartic anharmonic interactions comes only from the processes contributing to $\Delta_j^{(4b)}$ and is given by

$$\begin{aligned}\Gamma_j^{(4)}(\omega,T)=&\frac{96}{\hbar^2}\sum_{\mathbf{q}_1,j_1}\sum_{\mathbf{q}_2,j_2}\sum_{\mathbf{q}_3,j_3}|V(\mathbf{0},j;\mathbf{q}_1,j_1;\mathbf{q}_2,j_2;\mathbf{q}_3,j_3)|^2\\&\times\{[(n_1+1)(n_2+1)(n_3+1)-n_1n_2n_3][\delta(\omega-\omega_1-\omega_2-\omega_3)-\delta(\omega+\omega_1+\omega_2+\omega_3)]\\&+3[n_1(n_2+1)(n_3+1)-(n_1+2)n_2n_3][\delta(\omega+\omega_1-\omega_2-\omega_3)-\delta(\omega-\omega_1+\omega_2+\omega_3)]\}.\end{aligned} \tag{B4}$$

For brevity, we have used the following shorthand notations for the frequencies and the occupation number in the above equations:

$$\omega_i=\omega_{\mathbf{q}_i,j_i},\qquad i=1,2,3, \tag{B5}$$

$$n_i\equiv n_{\mathbf{q}_i,j_i}=\frac{1}{\exp(\beta\hbar\omega_{\mathbf{q}_i,j_i}-1)},\qquad i=1,2,3, \tag{B6}$$

with $\beta=1/k_{\mathrm{B}}T$.

We note that the line shift due to $\Delta_j^{(4a)}(T)$ can be positive or negative depending on the sign of the coupling constant $V^{(4)}(\mathbf{0},j;\mathbf{0},j;\mathbf{q}_1,j_1;-\mathbf{q}_1,j_1)$. The shift due to $\Delta_j^{(4c)}(T)$ can also be positive or negative, depending on the signs of the products of the four-phonon couplings constants $V^{(4)}(\mathbf{0},j;\mathbf{0},j;-\mathbf{q}_1,j_1;\mathbf{q}_1,j_2)V^{(4)}(\mathbf{q}_1,j_1;-\mathbf{q}_1,j_2;\mathbf{q}_3,j_3;-\mathbf{q}_3,j_3)$ which make the dominant contributions to the sums in Eq. (B3). As regards $\Delta_j^{(4b)}(\omega,T)$, although $|V^{(4)}(\mathbf{0},j;\mathbf{q}_1,j_1;\mathbf{q}_2,j_2;\mathbf{q}_3,j_3)|^2$ is always positive, as in the case of the cubic anharmonic shifts, the sums over the Cauchy principal parts corresponding to the different decay processes can also lead to line-shift contributions with anomalous temperature dependence for some of the modes. Thus, on the whole, the leading order line shifts arising from fourth-order anharmonic interactions have more possibilities for having anomalous temperature dependence than those from third-order anharmonic interactions. However, the confirmation of this requires an accurate computation of all the four-phonon coupling matrix elements.

Nevertheless, like the above discussion of the anharmonic effects arising from three-phonon coupling, it is instructive to examine what happens within a constant matrix element approximation when we replace the combinations of the four-phonon coupling constants that occur in the linewidth and line-shift functions with numbers that are independent of the phonon mode indices or the wave vectors.

Within such an approximation, the linewidth functions $\Gamma_j^{(4)}(\omega,T)$ in Eq. (B4) become the same for all phonon modes and are proportional to the three-phonon density of states (DOS) $D^{(3)}(\omega,T)$ given by

$$\begin{aligned}D^{(3)}(\omega,T)=&\sum_{\mathbf{q}_1,j_1}\sum_{\mathbf{q}_2,j_2}\sum_{\mathbf{q}_3,j_3}\{[(n_1+1)(n_2+1)(n_3+1)-n_1n_2n_3][\delta(\omega-\omega_1-\omega_2-\omega_3)-\delta(\omega+\omega_1+\omega_2+\omega_3)]\\&+3[n_1(n_2+1)(n_3+1)-(n_1+1)n_2n_3][\delta(\omega+\omega_1-\omega_2-\omega_3)-\delta(\omega-\omega_1+\omega_2+\omega_3)]\}.\end{aligned} \tag{B7}$$

Here again, the first term in Eq. (B7) is related to the down-conversion process where the high-energy phonon of interest decays into three phonons of lower energy. The second term in Eq. (B7) describes the up-conversion processes where the

phonon of interest absorbs a thermal phonon and emits two other phonons or absorbs two thermal phonons and emits a phonon of higher frequency.

Similarly, within the same approximation, all the line-shift functions $\Delta_j^{(4b)}(\omega, T)$ arising from the quartic anharmonic interactions become proportional to a single three-phonon kinematical function $P^{(3)}(\omega, T)$ given by

$$P^{(3)}(\omega,T) = \sum_{\mathbf{q}_1,j_1}\sum_{\mathbf{q}_2,j_2}\sum_{\mathbf{q}_3,j_3}\mathcal{P}\Bigg\{[(n_1+1)(n_2+1)(n_3+1)-n_1n_2n_3]\left(-\frac{1}{\omega+\omega_1+\omega_2+\omega_3}+\frac{1}{\omega-\omega_1-\omega_2-\omega_3}\right)$$
$$+3[n_1(n_2+1)(n_3+1)-(n_1+1)n_2n_3]\left(-\frac{1}{\omega-\omega_1+\omega_2+\omega_3}+\frac{1}{\omega+\omega_1-\omega_2-\omega_3}\right)\Bigg\}, \tag{B8}$$

where $\mathcal{P}$ denotes the Cauchy principal part. As earlier, the temperature dependence of $D^{(3)}(\omega, T)$ and $P^{(3)}(\omega, T)$ arises via the phonon occupancy factors n.

Figure 15 shows the three-phonon DOS $D^{(3)}(\omega, T)$ calculated at $T = 0, 35, 100$, and 300 K. The DFT-calculated frequencies of phonon modes M1–M10 are also marked in the plot. To get additional insights, we have plotted in Fig. 16 the separate contributions coming from the up- and down-conversion processes in $D^{(3)}(\omega, T)$ for the same four temperatures. We note that, unlike in the case of TDOS $D^{(2)}(\omega, T)$, the contributions from the up- and down-conversion channels in the case of three-phonon DOS $D^{(3)}(\omega, T)$ are comparable at higher temperatures. Furthermore, the high-frequency modes M6–M10 lie close to the peak of $D^{(3)}(\omega, T)$, as these modes have access to several combinations of the lower-frequency modes to decay into. On the other hand, the low-frequency modes M1–M3 have significant contributions only from up-conversion processes and only when the temperature is high enough.

Next, the frequency dependence of the three-phonon kinematical function $P^{(3)}(\omega, T)$ calculated at four different temperatures is shown in Fig. 17. Here again, phonon modes M1–M10 are marked by the arrows. We note that $P^{(3)}(\omega, T)$ is negative at all four temperatures for modes M1–M9, and even for M10, it is positive only at 300 K.

Within the constant matrix approximation, the temperature dependence of the quartic anharmonic line shifts for modes M1–M10 are readily calculated (up to unknown multiplicative constants arising from the matrix elements) and are shown in Figs. 18–20. The line shifts corresponding to the Hartree contributions, shown in Figs. 18 and 20, are the same for all modes. We have shown them for positive as well as negative values of the coupling matrix element combinations, as both signs are in principle possible; accordingly, as we remarked earlier, the temperature dependence of the Hartree line shifts can be normal or anomalous. In contrast, the contributions arising from $\Delta_j^{(4b)}(\omega, T)$ are proportional to $P^{(3)}[\omega_j(0), T]$ and hence still mode dependent. From Fig. 19, it is clear that these contributions to the line shifts for modes M1–M9 are negative and show a downward trend, corresponding to phonon softening with increasing temperature. On the other

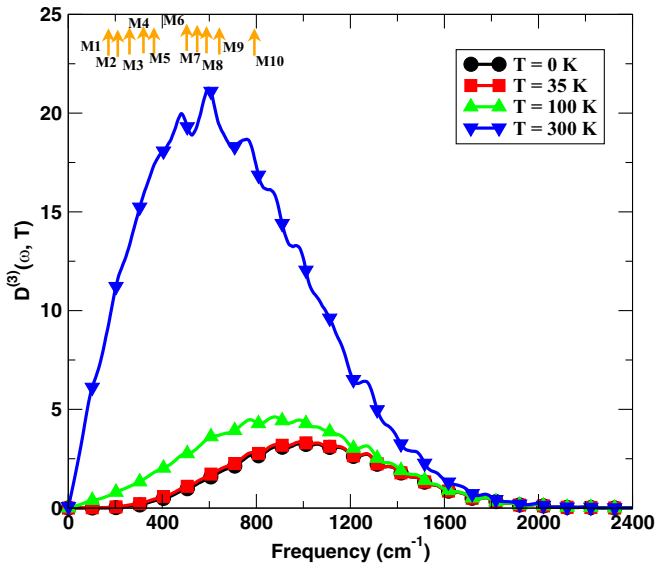

FIG. 15. Three-phonon density of states (DOS) of $Y_2Ti_2O_7$ calculated at four different temperatures. Modes M1–M10 are also marked. We note that $D^{(3)}(\omega, T)$ is almost the same at $T = 0$ and 35 K.

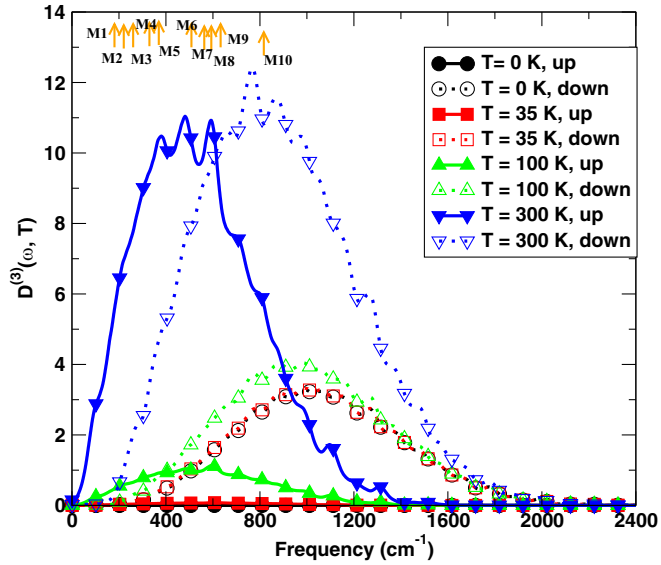

FIG. 16. The contribution of the up- and down-conversion decay processes to the three-phonon density of states (DOS) of $Y_2Ti_2O_7$ calculated at four different temperatures. Modes M1–M10 are also marked. We again note that the up-conversion contribution to $D^{(3)}(\omega, T)$ is almost negligible at $T = 0$ and 35 K, whereas the down-conversion contributions are almost the same at these temperatures.

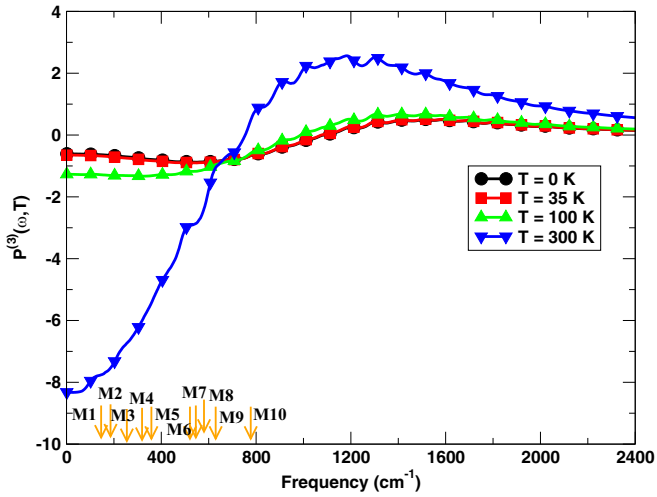

FIG. 17. Frequency dependence of the kinematical function $P^{(3)}(\omega, T)$ of $Y_2Ti_2O_7$ calculated at four different temperatures. For clarity, modes M1–M10 are also marked. We note that $P^{(3)}(\omega, T)$ is almost the same at $T = 0$ and 35 K.

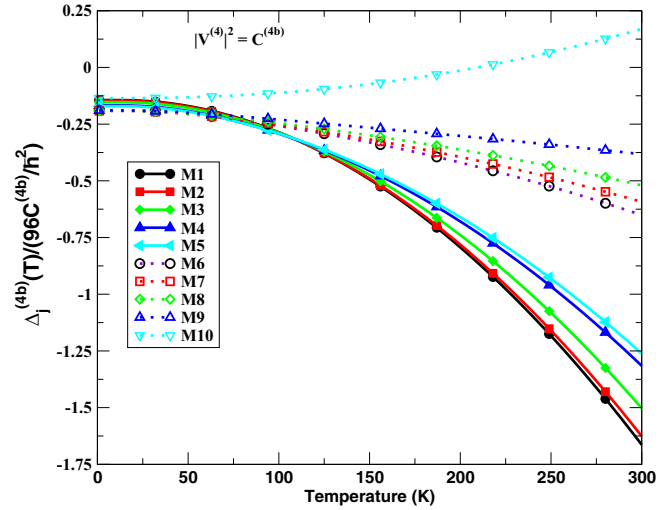

FIG. 19. Temperature dependence of the second-order line shifts arising from the quartic anharmonic interactions corresponding to Eq. (B2). Here, $|V^{(4)}(\mathbf{0}, j; \mathbf{q}_1, j_1; \mathbf{q}_2, j_2; \mathbf{q}_3, j_3)|^2$ is taken as a fixed number $C^{(4b)}$.

hand, the high-frequency mode M10, even though it is negative to start with, shows an upward trend with increasing temperature. This can further add to the anomalous behavior of mode M10 found in the cubic-anharmonic contributions. These features of Fig. 19 are, of course, fully consistent with the properties of the three-phonon kinematical function $P^{(3)}(\omega, T)$ shown in Fig. 17.

As in the previous Appendix, all the curves shown in Figs. 15–17 and 19 are based on calculations done at very many more points than those corresponding to the different symbols shown in these figures. The latter have been shown merely to help readers to distinguish between the different curves in the print version of this paper, where the colors would not be visible.

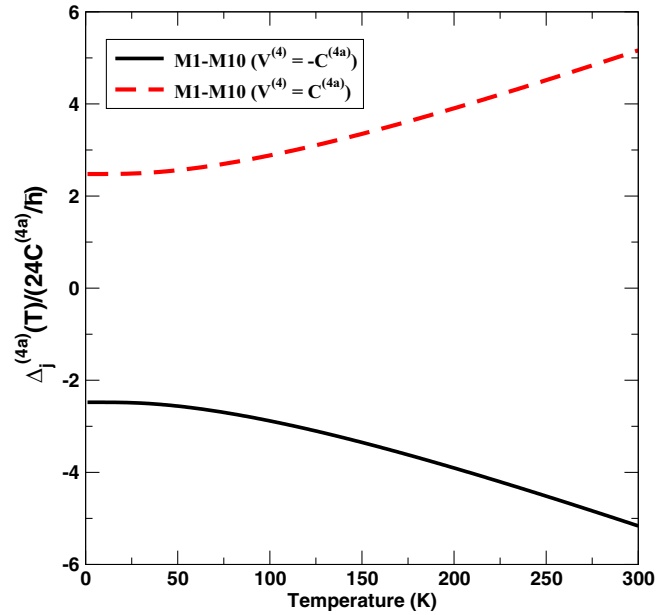

FIG. 18. Temperature dependence of the first-order Hartree contributions to the line shifts arising from the quartic anharmonic interactions [see Eq. (B1)]. Results are shown for positive (red dashed line) as well as the negative (black solid line) values of the four-phonon coupling constants when they are approximated as a single constant: $[V^{(4)}(\mathbf{0}, j; \mathbf{0}, j; \mathbf{q}_1, j_1; -\mathbf{q}_1, j_1) = C^{(4a)}]$. Within this assumption, the line shifts are the same for all modes M1–M10.

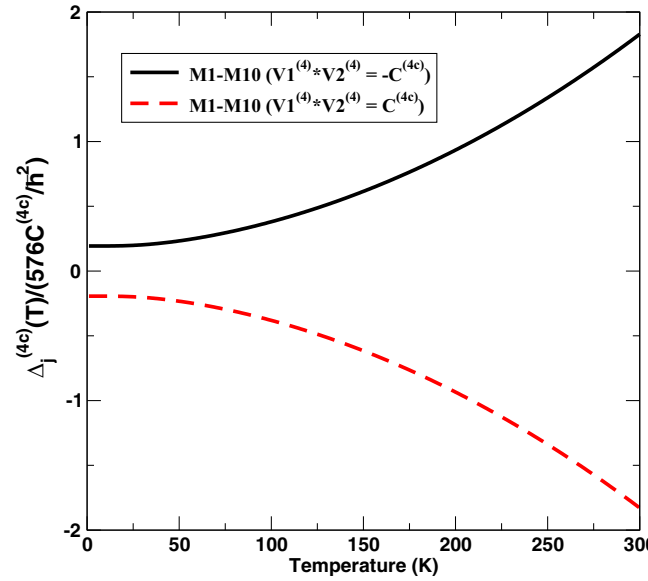

FIG. 20. Temperature dependence of the Hartree line shifts arising from the quartic anharmonic interactions treated to the second order [see Eq. (B3)]. Here again, the product of the four-phonon coupling constant is replaced by some effective average value $C^{(4c)}$, i.e., $V^{(4)}(\mathbf{0}, j; \mathbf{0}, j; -\mathbf{q}_1, j_1; \mathbf{q}_1, j_2)V^{(4)}(\mathbf{q}_1, j_1; -\mathbf{q}_1, j_2; \mathbf{q}_3, j_3; -\mathbf{q}_3, j_3) \rightarrow C^{(4c)}$. The results are shown for positive (red dashed line) as well as negative (black solid line) values of $C^{(4c)}$. Again, within this approximation, the shift is the same for all modes M1–M10.

[1] J. S. Gardner, M. J. P. Gingras, and J. E. Greedan, Magnetic pyrochlore oxides, Rev. Mod. Phys. **82**, 53 (2010).

[2] M. Subramanian, G. Aravamudan, and G. Subba Rao, Oxide pyrochlores—a review, Prog. Solid State Chem. **15**, 55 (1983).

[3] J. E. Greedan, Geometrically frustrated magnetic materials, J. Mater. Chem. **11**, 37 (2001).

[4] J. S. Gardner, S. R. Dunsiger, B. D. Gaulin, M. J. P. Gingras, J. E. Greedan, R. F. Kiefl, M. D. Lumsden, W. A. MacFarlane, N. P. Raju, J. E. Sonier *et al.*, Cooperative Paramagnetism in the Geometrically Frustrated Pyrochlore Antiferromagnet $Tb_2Ti_2O_7$, Phys. Rev. Lett. **82**, 1012 (1999).

[5] A. P. Ramirez, A. Hayashi, R. J. Cava, R. Siddharthan, and B. S. Shastry, Zero-point entropy in 'spin ice', Nature (London) **399**, 333 (1999).

[6] M. J. Harris, S. T. Bramwell, D. F. McMorrow, T. Zeiske, and K. W. Godfrey, Geometrical Frustration in the Ferromagnetic Pyrochlore $Ho_2Ti_2O_7$, Phys. Rev. Lett. **79**, 2554 (1997).

[7] S. Saha, S. Singh, B. Dkhil, S. Dhar, R. Suryanarayanan, G. Dhalenne, A. Revcolevschi, and A. K. Sood, Temperature-dependent raman and x-ray studies of the spin-ice pyrochlore $Dy_2Ti_2O_7$ and nonmagnetic pyrochlore $Lu_2Ti_2O_7$, Phys. Rev. B **78**, 214102 (2008).

[8] M. Mączka, M. L. Sanjuán, A. F. Fuentes, K. Hermanowicz, and J. Hanuza, Temperature-dependent Raman study of the spin-liquid pyrochlore $Tb_2Ti_2O_7$, Phys. Rev. B **78**, 134420 (2008).

[9] M. Mączka, J. Hanuza, K. Hermanowicz, A. F. Fuentes, K. Matsuhira, and Z. Hiroi, Temperature-dependent raman scattering studies of the geometrically frustrated pyrochlores $Dy_2Ti_2O_7$, $Gd_2Ti_2O_7$ and $Er_2Ti_2O_7$, J. Raman Spectrosc. **39**, 537 (2008).

[10] T. T. A. Lummen, I. P. Handayani, M. C. Donker, D. Fausti, G. Dhalenne, P. Berthet, A. Revcolevschi, and P. H. M. van Loosdrecht, Phonon and crystal field excitations in geometrically frustrated rare earth titanates, Phys. Rev. B **77**, 214310 (2008).

[11] C. Z. Bi, J. Y. Ma, B. R. Zhao, Z. Tang, D. Yin, C. Z. Li, D. Z. Yao, J. Shi, and X. G. Qiu, Far infrared optical properties of the pyrochlore spin ice compound $Dy_2Ti_2O_7$, J. Phys.: Condens. Matter **17**, 5225 (2005).

[12] F. X. Zhang, B. Manoun, S. K. Saxena, and C. S. Zha, Structure change of pyrochlore $Sm_2Ti_2O_7$ at high pressures, Appl. Phys. Lett. **86**, 181906 (2005).

[13] F. X. Zhang and S. K. Saxena, Structural changes and pressure-induced amorphization in rare earth titanates $RE_2Ti_2O_7$ (RE: Gd, Sm) with pyrochlore structure, Chem. Phys. Lett. **413**, 248 (2005).

[14] S. Saha, D. V. S. Muthu, C. Pascanut, N. Dragoe, R. Suryanarayanan, G. Dhalenne, A. Revcolevschi, S. Karmakar, S. M. Sharma, and A. K. Sood, High-pressure raman and x-ray study of the spin-frustrated pyrochlore $Gd_2Ti_2O_7$, Phys. Rev. B **74**, 064109 (2006).

[15] S. Singh, S. Saha, S. K. Dhar, R. Suryanarayanan, A. K. Sood, and A. Revcolevschi, Manifestation of geometric frustration on magnetic and thermodynamic properties of the pyrochlores $Sm_2X_2O_7 (X = \mathrm{Ti}, \mathrm{Zr})$, Phys. Rev. B **77**, 054408 (2008).

[16] S. Saha, D. V. S. Muthu, S. Singh, B. Dkhil, R. Suryanarayanan, G. Dhalenne, H. K. Poswal, S. Karmakar, S. M. Sharma, A. Revcolevschi *et al.*, Low-temperature and high-pressure raman and x-ray studies of pyrochlore $Tb_2Ti_2O_7$: phonon anomalies and possible phase transition, Phys. Rev. B **79**, 134112 (2009).

[17] M. Mączka, M. L. Sanjuán, A. F. Fuentes, L. Macalik, J. Hanuza, K. Matsuhira, and Z. Hiroi, Temperature-dependent studies of the geometrically frustrated pyrochlores $Ho_2Ti_2O_7$ and $Dy_2Ti_2O_7$, Phys. Rev. B **79**, 214437 (2009).

[18] J. S. Gardner, B. D. Gaulin, S.-H. Lee, C. Broholm, N. P. Raju, and J. E. Greedan, Glassy Statics and Dynamics in the Chemically Ordered Pyrochlore Antiferromagnet $Y_2Mo_2O_7$, Phys. Rev. Lett. **83**, 211 (1999).

[19] J. S. Gardner, B. D. Gaulin, A. J. Berlinsky, P. Waldron, S. R. Dunsiger, N. P. Raju, and J. E. Greedan, Neutron scattering studies of the cooperative paramagnet pyrochlore $Tb_2Ti_2O_7$, Phys. Rev. B **64**, 224416 (2001).

[20] J. E. Greedan, Frustrated rare earth magnetism: spin glasses, spin liquids and spin ices in pyrochlore oxides, J. Alloys Compd. **408–412**, 444 (2006), proceedings of Rare Earths '04 in Nara, Japan.

[21] R. Bianco, L. Monacelli, M. Calandra, F. Mauri, and I. Errea, Weak Dimensionality Dependence and Dominant Role of Ionic Fluctuations in the Charge-Density-Wave Transition of $NbSe_2$, Phys. Rev. Lett. **125**, 106101 (2020).

[22] P. Hohenberg and W. Kohn, Inhomogeneous electron gas, Phys. Rev. **136**, B864 (1964).

[23] W. Kohn and L. J. Sham, Self-consistent equations including exchange and correlation effects, Phys. Rev. **140**, A1133 (1965).

[24] P. Giannozzi, S. Baroni, N. Bonini, M. Calandra, R. Car, C. Cavazzoni, D. Ceresoli, G. L. Chiarotti, M. Cococcioni, I. Dabo *et al.*, QUANTUM ESPRESSO: A modular and open-source software project for quantum simulations of materials, J. Phys.: Condens. Matter **21**, 395502 (2009).

[25] D. R. Hamann, Optimized norm-conserving Vanderbilt pseudopotentials, Phys. Rev. B **88**, 085117 (2013).

[26] D. Vanderbilt, Soft self-consistent pseudopotentials in a generalized eigenvalue formalism, Phys. Rev. B **41**, 7892 (1990).

[27] D. M. Ceperley and B. J. Alder, Ground State of the Electron Gas by a Stochastic Method, Phys. Rev. Lett. **45**, 566 (1980).

[28] J. D. Pack and H. J. Monkhorst, "Special points for Brillouin-zone integrations"—a reply, Phys. Rev. B **16**, 1748 (1977).

[29] S. Baroni, S. de Gironcoli, A. Dal Corso, and P. Giannozzi, Phonons and related crystal properties from density-functional perturbation theory, Rev. Mod. Phys. **73**, 515 (2001).

[30] P. Giannozzi, S. de Gironcoli, P. Pavone, and S. Baroni, *Ab initio* calculation of phonon dispersions in semiconductors, Phys. Rev. B **43**, 7231 (1991).

[31] B. G. Pfrommer, M. Côté, S. G. Louie, and M. L. Cohen, Relaxation of crystals with the quasi-Newton method, J. Comput. Phys. **131**, 233 (1997).

[32] L. Paulatto, F. Mauri, and M. Lazzeri, Anharmonic properties from a generalized third-order *ab initio* approach: theory and applications to graphite and graphene, Phys. Rev. B **87**, 214303 (2013).

[33] A. Debernardi, S. Baroni, and E. Molinari, Anharmonic Phonon Lifetimes in Semiconductors from Density-Functional Perturbation Theory, Phys. Rev. Lett. **75**, 1819 (1995).

[34] G. Deinzer, G. Birner, and D. Strauch, *Ab initio* calculation of the linewidth of various phonon modes in germanium and silicon, Phys. Rev. B **67**, 144304 (2003).

[35] X. Gonze and J.-P. Vigneron, Density-functional approach to nonlinear-response coefficients of solids, Phys. Rev. B **39**, 13120 (1989).

[36] A. Debernardi and S. Baroni, Third-order density-functional perturbation theory: A practical implementation with applications to anharmonic couplings in Si, Solid State Commun. **91**, 813 (1994).

[37] M. T. Vandenborre, E. Husson, J. P. Chatry, and D. Michel, Rare-earth titanates and stannates of pyrochlore structure; vibrational spectra and force fields, J. Raman Spectrosc. **14**, 63 (1983).

[38] F. Brisse and O. Knop, Pyrochlores. III. X-ray, neutron, infrared, and dielectric studies of $A_2Sn_2O_7$ stannates, Can. J. Chem. **46**, 859 (1968).

[39] O. Knop, F. Brisse, and L. Castelliz, Pyrochlores. V. Thermoanalytic, x-ray, neutron, infrared, and dielectric studies of $A_2Ti_2O_7$ titanates, Can. J. Chem. **47**, 971 (1969).

[40] J. F. McCaffrey, N. T. McDevitt, and C. M. Phillippi, Infrared lattice spectra of rare-earth stannate and titanate pyrochlores, J. Opt. Soc. Am. **61**, 209 (1971).

[41] H. C. Gupta, S. Brown, N. Rani, and V. B. Gohel, Lattice dynamic investigation of the zone center wavenumbers of the cubic $A_2Ti_2O_7$ pyrochlores, J. Raman Spectrosc. **32**, 41 (2001).

[42] A. A. Maradudin and A. E. Fein, Scattering of neutrons by an anharmonic crystal, Phys. Rev. **128**, 2589 (1962).

[43] D. N. Zubarev, Double-time Green functions in statistical physics, Sov. Phys. Uspekhi **3**, 320 (1960).

[44] P. Thibaudeau, A. Debernardi, V. T. Phuoc, S. da Rocha, and F. Gervais, Phonon anharmonicity in disordered $MgAl_2O_4$ spinel, Phys. Rev. B **73**, 064305 (2006).

[45] M. Upadhyay Kahaly and U. V. Waghmare, Size dependence of thermal properties of armchair carbon nanotubes: A first-principles study, Appl. Phys. Lett. **91**, 023112 (2007).

[46] P. K. Verma, First principles study of the structural, electronic, elastic, mechanical, thermal, and vibrational properties in pyrochlores and temperature-dependent phonon properties in pyrochlores and $SrTiO_3$ perovskite, Ph.D. thesis, Indian Institute of Science, Bangalore, 2019, https://etd.iisc.ac.in/handle/2005/4468.

[47] A. J. C. Ladd, B. Moran, and W. G. Hoover, Lattice thermal conductivity: A comparison of molecular dynamics and anharmonic lattice dynamics, Phys. Rev. B **34**, 5058 (1986).

[48] L. Bohlin and T. Högberg, Anharmonic phonon shifts and widths for a centro symmetrical potential, J. Phys. Chem. Solids **29**, 1805 (1968).

[49] S. Kumar and H. Gupta, First principles study of zone centre phonons in rare-earth pyrochlore titanates, $RE_2Ti_2O_7$ (RE = Gd, Dy, Ho, Er, Lu; Y), Vib. Spectrosc. **62**, 180 (2012).

[50] M. Vandenborre and E. Husson, Comparison of the force field in various pyrochlore families. I. The $A_2B_2O_7$ oxides, J. Solid State Chem. **50**, 362 (1983).

[51] A. Fuentes, K. Boulahya, M. Maczka, J. Hanuza, and U. Amador, Synthesis of disordered pyrochlores, $A_2Ti_2O_7$ (A = Y, Gd and Dy), by mechanical milling of constituent oxides, Solid State Sci. **7**, 343 (2005).

[52] S. Brown, H. C. Gupta, J. A. Alonso, and M. J. Martinez-Lope, Vibrational spectra and force field calculation of $A_2Mn_2O_7$ (A = Y, Dy, Er, Yb) pyrochlores, J. Raman Spectrosc. **34**, 240 (2003).

[53] S. Saha, Phonon anomalies and phase transitions in pyrochlore titanates, boron nitride nanotubes and multiferroic $BiFeO_3$: Temperature- and pressure-dependent Raman studies, Ph.D. thesis, Indian Institute of Science, Bangalore, 2010, https://etd.iisc.ac.in/handle/2005/2244.

[54] F. Birch, Finite strain isotherm and velocities for single-crystal and polycrystalline nacl at high pressures and 300 °K, J. Geophys. Res.: Solid Earth **83**, 1257 (1978).

[55] P. R. Scott, A. Midgley, O. Musaev, D. V. Muthu, S. Singh, R. Suryanarayanan, A. Revcolevschi, A. K. Sood, and M. B. Kruger, High-pressure synchrotron x-ray diffraction study of the pyrochlores: $Ho_2Ti_2O_7$, $Y_2Ti_2O_7$ and $Tb_2Ti_2O_7$, High Press. Res. **31**, 219 (2011).

[56] J. M. Pruneda and E. Artacho, First-principles study of structural, elastic, and bonding properties of pyrochlores, Phys. Rev. B **72**, 085107 (2005).

[57] W. R. Panero, L. Stixrude, and R. C. Ewing, First-principles calculation of defect-formation energies in the $Y_2(Ti, Sn, Zr)_2O_7$ pyrochlore, Phys. Rev. B **70**, 054110 (2004).

[58] J. M. Farmer, L. A. Boatner, B. C. Chakoumakos, M.-H. Du, M. J. Lance, C. J. Rawn, and J. C. Bryan, Structural and crystal chemical properties of rare-earth titanate pyrochlores, J. Alloys Compd. **605**, 63 (2014).

[59] J. K. Gill, O. Pandey, and K. Singh, Role of sintering temperature on thermal, electrical and structural properties of $Y_2Ti_2O_7$ pyrochlores, Int. J. Hydrogen Energy **36**, 14943 (2011), fuel Cell Technologies: FUCETECH 2009.

[60] U. Matsumoto, T. Ogawa, C. A. J. Fisher, S. Kitaoka, and I. Tanaka, Cooperative oxide-ion transport in pyrochlore $Y_2Ti_2O_7$: A first-principles molecular dynamics study, J. Phys. Chem. C **125**, 20460 (2021).

[61] A. Otero-de-la-Roza, D. Abbasi-Pérez, and V. Luaña, GIBBS2: a new version of the quasiharmonic model code. II. Models for solid-state thermodynamics, features and implementation, Comput. Phys. Commun. **182**, 2232 (2011).

[62] T. Lan, C. W. Li, and B. Fultz, Phonon anharmonicity of rutile SnO_2 studied by Raman spectrometry and first principles calculations of the kinematics of phonon-phonon interactions, Phys. Rev. B **86**, 134302 (2012).

[63] M. Balkanski, R. F. Wallis, and E. Haro, Anharmonic effects in light scattering due to optical phonons in silicon, Phys. Rev. B **28**, 1928 (1983).

[64] I. P. Ipatova, A. A. Maradudin, and R. F. Wallis, Temperature dependence of the width of the fundamental lattice-vibration absorption peak in ionic crystals. II. Approximate numerical results, Phys. Rev. **155**, 882 (1967).